

Periodicity from X-ray sources within the inner Galactic disk

Samaresh Mondal¹, Gabriele Ponti^{1,2}, Tong Bao³, Frank Haberl², Sergio Campana¹, Charles J. Hailey⁴, Shifra Mandel⁴, Sandro Mereghetti⁵, Kaya Mori⁴, Mark R. Morris⁶, Nanda Rea^{7,8}, and Lara Sidoli⁵

¹INAF – Osservatorio Astronomico di Brera, Via E. Bianchi 46, 23807 Merate (LC), Italy e-mail: samaresh.mondal@inaf.it

²Max-Planck-Institut für extraterrestrische Physik, Gießenbachstraße 1, 85748, Garching, Germany

³School of Astronomy and Space Science, Nanjing University, Nanjing 210046, China

⁴Columbia Astrophysics Laboratory, Columbia University, Columbia, NY, 10027, USA

⁵INAF – Istituto di Astrofisica Spaziale e Fisica Cosmica, via A. Corti 12, 20133 Milano, Italy

⁶Department of Physics and Astronomy, University of California, Los Angeles, CA, 90095-1547, USA

⁷Institute of Space Sciences (ICE, CSIC), Campus UAB, Carrer de Can Magrans s/n, E-08193 Barcelona, Spain

⁸Institut d’Estudis Espacials de Catalunya (IEEC), Carrer Gran Capità 2–4, 08034 Barcelona, Spain

Received XXX; accepted YYY

ABSTRACT

Aims. For many years it had been claimed that the Galactic ridge X-ray emission at the Galactic Center (GC) is truly diffuse in nature. However, with the advancement of modern X-ray satellites, it has been found that most of the diffuse emission actually comprises thousands of previously unresolved X-ray point sources. Furthermore, many studies suggest that a vast majority of these X-ray point sources are magnetic cataclysmic variables (CVs) and active binaries. One unambiguous way to identify these magnetic CVs and other sources is by detecting their X-ray periodicity. Therefore, we systematically searched for periodic X-ray sources in the inner Galactic disk, including the GC region.

Methods. We used data from our ongoing *XMM-Newton* Heritage Survey of the inner Galactic disk ($350^\circ \lesssim l \lesssim +7^\circ$ and $-1^\circ \lesssim b \lesssim +1^\circ$) plus archival *XMM-Newton* observations of the GC. We computed the Lomb-Scargle periodogram for the soft (0.2–2 keV), hard (2–10 keV), and total (0.2–10 keV) band light curves to search for periodicities. Furthermore, we modeled the power spectrum using a power-law model to simulate 1000 artificial light curves and estimate the detection significance of the periodicity. We fitted the energy spectra of the sources using a simple power-law model plus three Gaussians, at 6.4, 6.7, and 6.9 keV, for the iron *K* emission complex.

Results. We detected periodicity in 26 sources. For 14 of them, this is the first discovery of periodicity. For the other 12 sources, we found periods similar to those already known, indicating no significant period evolution. The intermediate polar (IP) type sources display relatively hard spectra compared to polars. We also searched for the *Gaia* counterparts of the periodic sources to estimate their distances using the *Gaia* parallax. We found a likely *Gaia* counterpart for seven sources.

Conclusions. Based on the periodicity, hardness ratio, and the equivalent width of Fe *K* line emission, we have classified the sources into four categories: IPs, polars, neutron star X-ray binaries, and unknown. Of the 14 sources for which we detect the periodicity for the first time, four are likely IPs, five are likely polars, two are neutron star X-ray binaries, and three are of an unknown nature.

Key words. X-rays:binaries – Galaxy:center – Galaxy:disk – white dwarfs – pulsars – novae, cataclysmic variables

1. Introduction

In order to understand the star formation history of our Galaxy, it is important to know the number of stars that ended their main-sequence life long ago. Compact remnants of dead stars, such as black holes, neutron stars (NSs), and white dwarfs (WDs), are commonly found in binary systems and are visible in X-rays. Accreting WD binaries are the most common type of remnant in our Galaxy as WDs are the end product of intermediate- and low-mass stars. Many of these low-mass stars are born in binary systems with small separations that go through one or more mass transfer phase, leading to the formation of cataclysmic variables (CVs). More than a thousand CVs have been found in the solar neighborhood (Downes et al. 2001; Ritter & Kolb 2003). CVs are categorized as magnetic or nonmagnetic (see Cropper 1990; Patterson 1994; Mukai 2017, for a review). Magnetic CVs are primarily categorized into two subtypes: polar and intermediate polar (IP). Polars have a very strong magnetic field (> 10 MG), which synchronizes the spin and orbital motion (i.e., $P_{\text{spin}} = P_{\text{orb}}$). The high magnetic field in polars is confirmed by

the observation of strong optical polarization and the measurement of cyclotron humps (Warner 2003). In polars, the accretion directly follows the magnetic field lines from the L1 point, and no accretion disk is formed. IPs have a relatively weak surface magnetic field of 1 – 10 MG; therefore, they have less synchronization, and an accretion disk is created. In these systems, the material leaving the L1 point forms an accretion disk until the magnetic pressure becomes equal to the ram pressure of the accreting gas. The X-ray emission from CVs originates from close to the magnetic pole. The accreting material follows the magnetic field lines, and as it approaches the WD surface, the radial in-fall velocity reaches supersonic speeds of 3000–10000 km s⁻¹. A shock front appears above the WD surface, and the in-falling gas releases its energy in the shock, resulting in hard X-ray photons (Aizu 1973; Saxton et al. 2005).

Early observations of the Galactic Center (GC) revealed a diffuse X-ray emission (Worrall et al. 1982; Warwick et al. 1985; Yamauchi et al. 1996) called Galactic ridge emission. For many years a central point of debate has been whether the Galactic

ridge emission is truly diffuse or composed of emission from many unresolved X-ray point sources. The advent of modern X-ray satellites such as *XMM-Newton* and *Chandra* opened up the possibility of detecting very faint X-ray sources in crowded regions such as the inner GC. This is not possible in the optical waveband due to the high extinction toward the GC. A deep *Chandra* observation of the inner Galactic bulge has demonstrated that more than 80% of the Galactic ridge emission is produced by CVs and coronally active stars (Wang et al. 2002; Revnivtsev et al. 2009; Munro et al. 2003a, 2009; Zhu et al. 2018). Although this strongly indicates that a large fraction of the X-ray sources observed toward the GC are magnetic CVs, the physical nature of CVs in the GC remains unclear. Moreover, it was suggested that, based on the hard power-law-type spectral shape and the emission of Fe *K* complex lines, the majority are IPs (Munro et al. 2004)

The Galactic ridge X-ray emission displays a copious amount of lines from ionized iron at 6.7 and 6.9 keV. Some studies that compared the stellar mass distribution with the Fe XXV (6.7 keV) line intensity map suggest the presence of truly diffuse hard X-ray emission (Uchiyama et al. 2011b; Nishiyama et al. 2013; Yasui et al. 2015). However, a recent study by our group found that this diffuse hard emission in the GC can be explained if one assumes that the GC stellar population has iron abundances ~ 1.9 times higher than those in the Galactic bar/bulge (Anastasopoulou et al. 2023). Furthermore, the 20–40 keV emission from the GC observed by *NuSTAR* is best explained by two-temperature plasma models with $kT_1 \sim 1$ keV and $kT_2 \sim 7.5$ keV. The ~ 1 keV temperature component is attributed to emission from supernovae heating the interstellar medium, coronally active stars, and nonmagnetic WDs (Revnivtsev et al. 2009). The ~ 7.5 keV temperature component is thought to be produced by emission from resolved and unresolved accreting IPs (Perez et al. 2015). An additional component with a higher plasma temperature, $kT \sim 35$ keV (Hailey et al. 2016), was recently measured. In addition, Munro et al. (2003b) reported the discovery of eight periodic sources in a $17' \times 17'$ field of the GC. Their periods range from 300 s to 4.5 hr. All these sources exhibit hard power-law-type spectral shapes (with photon index $\Gamma \sim 0$) and 6.7 keV iron-line emission. These properties are consistent with magnetically accreting magnetic CVs.

We are in the process of performing an X-ray scan of the inner Galactic disk using *XMM-Newton* (Jansen et al. 2001; PI: G. Ponti). The main aim of this survey is to constrain the flow of hot baryons that feed large-scale energetic events such as the Galactic chimneys (Ponti et al. 2019, 2021), the *Fermi* bubbles (Su et al. 2010), and the eROSITA bubbles (Predehl et al. 2020). In early 2021, while performing this survey, we detected an X-ray source with periodic modulation at 432 s (Mondal et al. 2022). The source was previously observed by *Suzaku* in 2008 (Uchiyama et al. 2011a) and classified as an IP. Furthermore, while examining *XMM-Newton* archival observations, we discovered periodicity in two other sources within $1^\circ 5'$ of the GC (Mondal et al. 2023). These two sources are also classified as IPs based on the detected spin period and detection of an iron emission complex in the spectra. Therefore, we took a systematic approach to hunt for such periodic X-ray sources that might help us classify them. In this paper we report the discoveries obtained from a periodicity search using *XMM-Newton* observations of the Galactic disk and the GC.

2. Observations and data reduction

We have almost completed one side of the Galactic disk extending from $l \geq 350^\circ$ to $l \leq +1.5^\circ$ (see Fig. 1). The survey has an exposure of 20 ks per tile and is expected to cover the Galactic disk region in the range $350^\circ < l < +7^\circ$ and $-1^\circ < b < +1^\circ$. During this campaign, we detected thousands of X-ray point sources of various types. A forthcoming paper will present a sample study of the X-ray point sources. Here we are focusing on X-ray sources that show periodic modulations. While doing this analysis, we considered including the GC region for positional comparison of the sources located in the disk and GC (Ponti et al. 2013, 2015). For the GC, we used the *XMM-Newton* archival observations. In total, we analyzed 444 *XMM-Newton* observations, including our Galactic disk scanning observations plus the archival observations of the GC. The observation data files were processed using the *XMM-Newton* Science Analysis System (SAS, v19.0.0)¹. We used the task `evselect` to construct a high energy background light curve (energy between 10 and 12 keV for EPIC-pn and above 10 keV for EPIC-MOS1 and MOS2) by selecting only `PATTERN==0`. The background light curve was used to filter high background flaring activity and create good time intervals. We used the SAS task `emldetect` for point source detection and source list creation. For each individual detector, EPIC-pn, MOS1, or MOS2 (Strüder et al. 2001; Turner et al. 2001), the source detection was performed in five energy bands: 0.2–0.5 keV, 0.5–1 keV, 1–2 keV, 2–4 keV, and 4–12 keV for a given single observation. The source detection algorithm separately provides net counts and maximum likelihood values for the five energy bands and three detectors: EPIC-pn, MOS1, and MOS2. The source detection tool also provides the keyword `EXT` value that indicates whether the emission is from a point-like or extended source. We chose `EXT = 0` to select the point sources only. The total number of point sources detected in our survey is ~ 50000 . Then, we applied a filter in which only sources with a total number of counts (EPIC-pn+MOS1+MOS2) higher than 200 were chosen. This resulted in 2500 point sources for which we extracted the light curves using the SAS task `evselect` after applying the Solar System barycenter correction to the event files using the SAS task `barycen`. We only selected events with `PATTERN \leq 4` and `PATTERN \leq 12` for EPIC-pn and the MOS1 and MOS2 detectors, respectively. We chose a circular region of $20''$ radius for the source products extraction. The background products were extracted from an annular region centered on the source position with inner and outer radii of $25''$ and $30''$, respectively. The spectra were binned to have a minimum of 20 counts in each energy bin. Many fields of the GC have been observed more than once. If a source has been observed multiple times, we searched for pulsations in each observation individually.

3. Results

3.1. Period search

The *XMM-Newton* observations suffer from gaps due to the filtering of high background flaring activities. As the *XMM-Newton* observations suffer from gaps, we used the Lomb-Scargle periodogram (Lomb 1976; Scargle 1982), which is well known for detecting periodic signals in unevenly sampled time series data. We computed the false alarm probability to estimate the statistical significance of the periodogram peaks. The false alarm probability obtained is based on the analytical approximation proposed by Baluiev (2008), which employs extreme value

¹ <https://www.cosmos.esa.int/web/xmm-newton/sas>

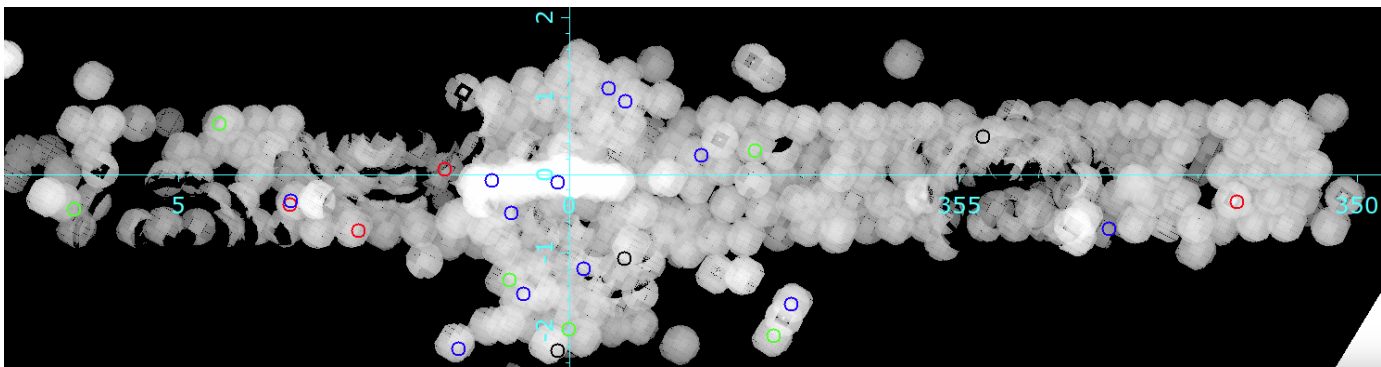


Fig. 1: Mosaic of the exposure maps created using the ongoing *XMM-Newton* observations of the Galactic disk plus archival observations of the GC. The small red, blue, and green circles show the positions of confirmed or likely NSs, IPs, and polars, respectively. The black circles indicate the unclassified sources.

statistics to compute an upper bound of the false alarm probability (or a lower limit of the significance of the detected periodicity). For our timing analysis, we used the PYTHON-based *astropy* (Astropy Collaboration et al. 2013, 2018, 2022) package’s time-series module².

We extracted the light curves in three different bands (0.2–2, 2–10, and 0.2–10 keV) for the three EPIC detectors (pn, MOS1, and MOS2). The light curves were extracted with a time bin of 74 ms for the EPIC-pn and 3 s for the MOS1 and MOS2 detectors in full frame mode of observation. The Lomb-Scargle periodogram was computed for all nine light curves of each source, and a periodicity search was conducted. The EPIC-pn detector has a frame time of 74 ms, which allowed us to probe a maximum frequency of ~ 6 Hz, whereas in the case of the MOS1 and MOS2 detectors, we were able to probe a maximum frequency of ~ 0.16 Hz. We imposed the criterion that the periodicity detected at a frequency below 0.16 Hz should be present in all three detectors. To search for periodicity at a higher frequency within the range 0.16–6 Hz, we used only the data from EPIC-pn. We have detected periodicity at a significance above 3σ in 23 sources. Possible periodicities with significance between 2 and 3σ were found in another three sources³. Figures A.1 and A.2 show the Lomb-Scargle periodograms of the 26 sources, with the horizontal lines indicating the detection significance levels.

Figure 1 shows the mosaic of the exposure maps created from our ongoing *XMM-Newton* observations of the Galactic disk plus the *XMM-Newton* archival observations of the GC. The small circles indicate the positions of the periodic sources. We have completed the survey of one side of the Galactic disk extending to $\sim 350^\circ$; however, most pulsators are concentrated near the GC.

Table A.1 shows the details of the X-ray properties of the periodic sources. The period column shows the pulsation period obtained in our analysis and compares it with the previously reported period. The pulse fraction is computed in 2–10 keV bands. The name of the sources is taken from the 4XMM catalog except for the sources XMMU J173029.8–330920, XMMU J175441.9–265919, and XMMU J180140.3–23422, which were not listed in the 4XMM (Webb et al. 2020) archive as these sources were first detected in our campaign. The X-ray position and 1σ positional error of the sources are taken from the

4XMM catalog. We also list the source type based on previous studies, and for sources that were not classified before, we give a tentative classification based on the X-ray period, hardness ratio (HR) values, and spectral properties. Figure 2 shows the distribution of the log of pulse period for various source types. Figure 3 shows the distribution of pulse fraction for the different categories. The pulse fraction was computed as $PF = \frac{F_{\max} - F_{\min}}{F_{\max} + F_{\min}}$, where F_{\max} and F_{\min} are the maximum and minimum counts in the folded light curves, respectively. For sources with more than one *XMM-Newton* observation, we report the periodicity from the multiple observations in Tables A.2 and A.3.

3.2. Caveats for the false alarm probability

Accretion-powered systems such as CVs and X-ray binaries are known to exhibit aperiodic variability over a wide range of timescales. This irregularity, often referred to as “red noise,” constitutes a significant aspect of aperiodic variability and has the potential to introduce spurious periodic signals, especially at lower frequencies (Warner 1989). Consequently, it is essential to assess the likelihood of false detections among these periodic signals found with the Lomb-Scargle periodogram method by using a large simulated dataset (Bao & Li 2022).

Specifically, we employed a power-law model to characterize the source power spectrum, which has the form of

$$P(\nu) = N\nu^{-1} + C_p. \quad (1)$$

In this equation, N represents the normalization factor, and C_p accounts for the Poisson noise, which is influenced by the mean photon flux of the source.

To begin, we estimated the power spectral density (PSD) using the standard periodogram approach with an $[\text{rms}/\text{mean}]^2$ PSD normalization (Vaughan et al. 2003). However, as mentioned in Section 3.1, some of the light curves suffer from gaps due to background flares. For these cases, we filled the gap with artificial light curves of Poisson noise, assuming the mean flux is consistent with that of the source. Although such processing results in little differences in the described PSDs, for most of the periodic sources here these gaps are fortunately negligible in terms of time (i.e., they take less than 0.5% of the total exposure time). Only one case exhibits a significant data gap, which takes $\sim 1.4\%$ of the single observation, with ObsID=0783160101. This source (4XMM J174816.9–280750) consistently exhibits the same periodic signal across multiple observations (see Table A.3). Thus, the possible uncertainty of its confidence estimation

² <https://docs.astropy.org/en/stable/timeseries/index.html>

³ We also detected a few sources with detection significance of the pulsation just above the 1σ confidence level. We did not list these sources in Table A.1; one such example is the transient Galactic bulge IP XMMU J175035.2–293557 (Hofmann et al. 2018).

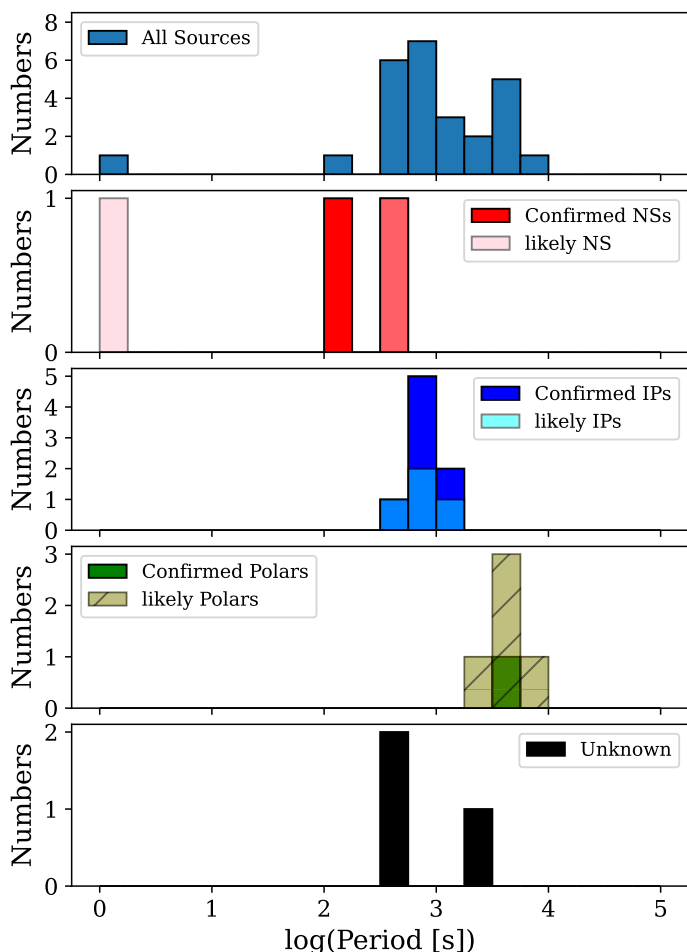


Fig. 2: Distribution of $\log(\text{period})$ for various source types.

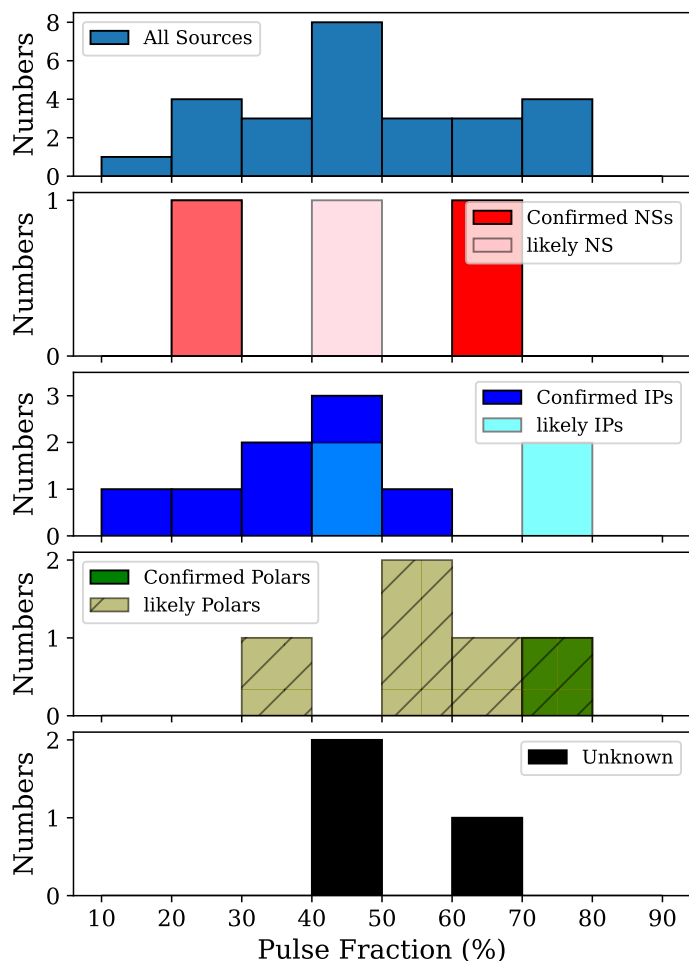


Fig. 3: Distribution of the 2-10 keV pulse fraction in percent for different source types.

by the process of filling gaps will not impact the verification of its periodicity.

We fitted the power spectrum of each source with Eq. 1, using the maximum likelihood function discussed in Vaughan (2010) and the Markov chain Monte Carlo approach, employing the Python package *emcee*⁴ (Foreman-Mackey et al. 2013) to derive the best-fit parameters and their associated uncertainties.

It turns out that only three of the periodic sources could be adequately described by the power-law model with constrained normalization, implying a potential influence of red noise. For the remaining sources, Poisson noise actually dominates the source power spectrum. Thus, for the source with potential red noise, simulated light curves for this best-fit power-law model were constructed using the method of Timmer & Koenig (1995), which were resampled and binned to have the same duration, mean count rate, and variance as the observed light curve. As for sources where Poisson noise prevailed, we followed a similar procedure to simulate their light curves, assuming pure Poisson noise. A group of 1000 simulated time series was produced for each source. To evaluate the false alarm level, we computed the maximum Lomb-Scargle power for each simulated light curve. Specifically, we considered the top 0.3% of the maximum Lomb-Scargle power from the 1000 Lomb-Scargle periodograms, corresponding to the 3σ confidence level estimation, and the top 5% as the threshold corresponding to 2σ (approximately 95%). These simulated thresholds were then over-

laid on the Lomb-Scargle periodogram (Figs. A.1 and A.2), and the confidence levels, calculated using Baluev’s analysis method (Baluev 2008), were compared. It turns out that 23 sources exceed the simulated-based threshold of 3σ , and 17 of them exceed the 3σ threshold of Baluev’s method. The deviation between these two is mainly due to that the Baluev method, by design, provides an upper limit to the false alarm probability with little overestimation (Baluev 2008).

3.3. Period and pulse fraction distribution

The top panel of Fig. 2 shows the period distribution of sources in our sample. The distribution has two peaks at around ~ 800 s and ~ 4800 s. The first peak is associated with the population of IPs, and the second peak corresponds to the population of polars.

The spin period of NS and likely NS systems in our sample ranges from 1.36 s to 411.3 s. The spin period of Galactic NS high-mass X-ray binaries (HMXRBs) ranges from a few to thousands of seconds, and the distribution has peaks around ~ 250 s (Neumann et al. 2023). The red histogram in the top panel of Fig. 2 shows the distribution of the period for NS X-ray binaries in our sample.

The blue and cyan histogram in the middle panel of Fig. 2 shows the period distribution for the known IPs plus the tentative identification of IPs in our sample. The distribution has a peak of around 607 s. Typically, the spin period of IPs ranges between

⁴ <https://emcee.readthedocs.io/en/stable/>

30 s and 3000 s, with a peak near 1000 s (Scaringi et al. 2010). The middle panel of Fig. 3 (blue and cyan histogram) shows the distribution of pulse fraction for IPs. The pulse fraction ranges from 10% to 80% with a peak near 45%. One prominent feature in IPs is that the pulse fraction or the modulation depth typically increases with decreasing X-ray energy. This has been thought to be the effect of photoelectric absorption (Norton & Watson 1989). The distribution of pulse fraction of IPs covers a wide range of scales and can vary from a few percent up to $\sim 100\%$ with an average around 24% (Norton & Watson 1989; Haberl & Motch 1995).

In polars, the spin and orbital periods are synchronized, ranging from 3000 s to 30000 s (Scaringi et al. 2010). In our sample, the periods of polars vary from 4093 s to 6784 s, with the peak at ~ 4800 s. The light curves of polars show constant modulation of depth with X-ray energies. The depths are generally higher compared to IPs (Norton & Watson 1989). In the middle panel of Fig. 3, it is evident that the pulse fraction for polars starts at higher values, around 30% compared to IPs, and that more polar type sources are found between 50% and 60%.

3.4. Spectral modeling

We performed time-averaged spectral modeling using the X-ray spectral fitting software *xspec*⁵ (Arnaud 1996). We employed χ^2 statistics in our model fitting. The spectra were fitted using a simple model composed of a power law and three Gaussian lines (tbabs(power-law+g1+g2+g3)). The Galactic absorption component is represented by tbabs (Wilms et al. 2000). For the continuum, we used a simple power-law model, and g1, g2, and g3 represent the three Gaussian lines at 6.4, 6.7, and 6.9 keV, respectively, for iron emission complex. While doing the fit, we freeze the line energies at the expected values, and the width of the lines is fixed at zero eV. We jointly fit the spectra of EPIC-pn, MOS1, and MOS2 detectors. While fitting the spectra, we included a constant factor for cross-calibration uncertainty, which is fixed to unity for EPIC-pn and allowed for variation for MOS1 and MOS2. The spectral fitting results are summarized in Table A.4, and Figs. A.3 and A.4 show the fitted spectra of the sources.

Figure 4 shows the distribution of absorption column density N_H obtained from the X-ray spectral fitting. Overall, the N_H distribution has a peak near 10^{22} cm⁻², and more than 50% of the sources have N_H between $10^{21} - 3.16 \times 10^{22}$ cm⁻². There are three sources with high $N_H > 10^{23}$ cm⁻². The source 4XMM J175327.8–295716 has $N_H = 7 \times 10^{20}$ cm⁻², the lowest in our sample, which might indicate that this source is the closest to us among our sample or has a soft component that mimics the low N_H .

Figure 5 shows the distribution of photon index Γ . The distribution has a peak at $\Gamma \sim 0.6$. More than 50% of the sources have a flat spectral shape with $\Gamma < 1$. A significant number of sources in our sample have a softer spectrum with $\Gamma > 1.2$. We noticed that the majority of sources with high Γ values do not show any iron emission complex lines; only two of the seven sources with $\Gamma \geq 1.3$, show strong emission lines in the 6–7 keV band.

3.5. Gaia counterparts

A correct estimate of the distance to the source is required to derive their luminosity. For this, we searched for counterparts in the *Gaia* DR3 catalog. For each X-ray source, we computed

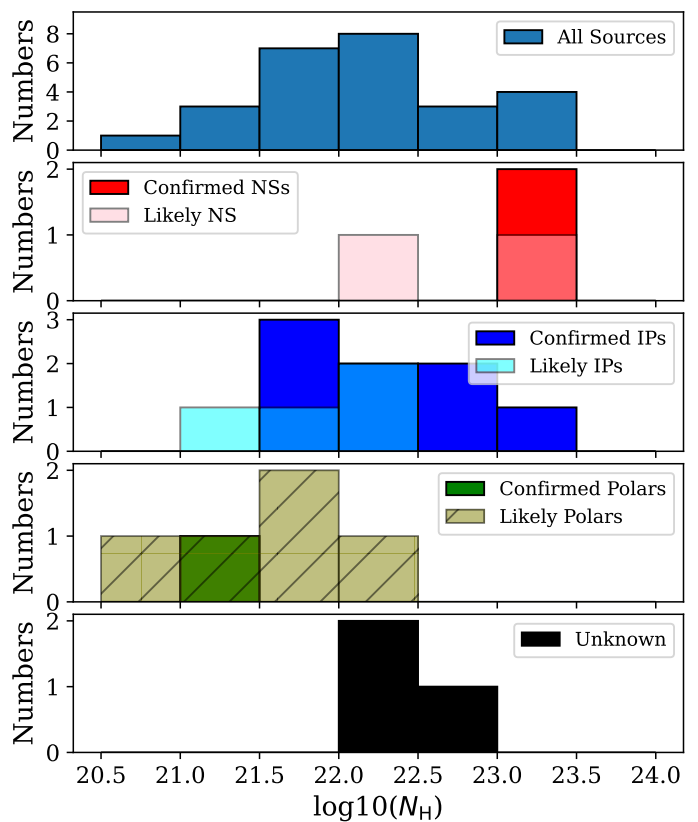


Fig. 4: Distribution of the absorption column density, N_H , for different source types.

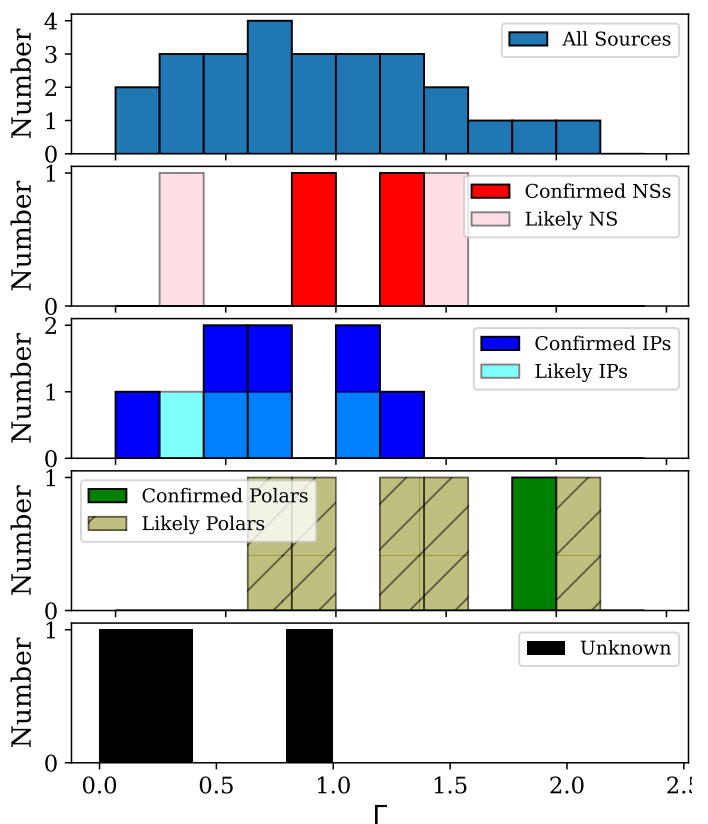


Fig. 5: Distribution of the photon index, Γ , for different source types.

⁵ <https://heasarc.gsfc.nasa.gov/xanadu/xspec/>

the *Gaia* source density by counting the number of *Gaia* sources within a circle of $1'$ radius at the source position. The *Gaia* density of sources is low and varies from 0.01 – 0.1 arcsec $^{-2}$. We compute the probability of the sources having a spurious association by multiplying the *Gaia* source density with the area associated with the *XMM-Newton* positional error. Table 1 lists the sources for which we found a *Gaia* counterpart within the 3σ positional uncertainty of *XMM-Newton*. We found a likely *Gaia* counterpart for seven *XMM-Newton* sources. If a counterpart is found, then we use the *Gaia* source ID to find the distance to the source from Bailer-Jones et al. (2021). The distance to the sources for which a *Gaia* counterpart was found varies from ~ 1.5 to ~ 5 kpc and the X-ray luminosity is in the range $5 \times 10^{32} - 6 \times 10^{33}$ erg s $^{-1}$.

4. Discussion

4.1. Typical properties of different classes of sources

We analyzed 444 *XMM-Newton* observations of the GC and the Galactic disk. We extracted X-ray light curves from nearly 2500 sources and systematically searched for X-ray pulsation. We detected periodicity in 26 sources, 14 of which are reported here for the first time. Many of the GC sources have a luminosity of a few times 10^{32} erg s $^{-1}$ (Muno et al. 2003a), which is comparable to the luminosity typically observed in bright magnetic CVs (Verbunt et al. 1997; Ezuka & Ishida 1999). NS HMXRBs have much higher luminosity and are detected during their outburst period, reaching luminosities up to 10^{38} erg s $^{-1}$. For the majority of the sources we did not find a *Gaia* counterpart due to the high absorption column density toward the GC and disk. Hence, the X-ray luminosity cannot be derived for a large number of sources and we cannot use this information to classify them. The NS HMXRBs are far less common in our Galaxy than the magnetic CVs. The nature of the Galactic sources is a long-standing question. Identifying the magnetic CVs or NS HMXRBs from X-ray periodicity alone can be difficult, as both types of sources usually display periods in a similar range. The short-period modulation in the X-ray light curve is thought to have originated from the spin period of the magnetically accreting WD or NS. In our sample, the smallest detected period is 1.36 s, and the maximum period detected is around 6784 s. The sample has a median period of 672 s. The pulse fraction of the modulation ranges from 10% to 80%. The detected periods are consistent with those of magnetic CVs and NSs in HMXRBs. A sample study of magnetic CVs indicates the median spin period is 6000 s (Ritter & Kolb 2003). There are also a few magnetic CVs with very short spin periods; for example, CTCV J2056–3014 has a spin period of 29.6 s (Lopes de Oliveira et al. 2020), and V1460 Her has a spin period of 38.9 s (Ashley et al. 2020). The spin periods of polars are mostly beyond 1 hr, while almost all IPs have WD spin periods lower than 1 hr. In contrast, 85 Galactic HMXRB pulsars (both with Be and OB supergiant companions) have a median (mean) spin period of 187 s (~ 970 s), with only four sources showing a period longer than 1 hr (Neumann et al. 2023).

It is evident that the different classes of sources (NS HMXRBs and magnetic CVs) exhibit a wide range of spin periods. Therefore, from the periodicity alone, it is difficult to understand the nature of the unclassified sources. Below we summarize a scheme to characterize the different classes of periodic X-ray sources utilizing their X-ray spectral, timing properties, and luminosity.

4.1.1. NS HMXRBs

The NS HMXRBs have properties that are very similar to IPs and they typically have very hard spectra. Figure 6 shows the period versus HR plot for classified and unclassified sources in our sample. The HR is calculated using the net counts in the 2–5 keV and 5–10 keV bands. We did not choose an energy band below 2 keV simply because it would be affected by Galactic absorption. The known NS HMXRBs appear very hard, similar to IPs; however, it is clear from Fig. 7 that they emit very little 6.7 keV iron line as compared to IPs. In almost all NS HMXRBs, the dominant component of the Fe K emission complex is the neutral 6.4 keV line emission and little to no ionized 6.7 and 6.9 keV line emission. This is because HMXRBs are mainly wind-fed systems, so the fluorescent iron line emission from the wind of the companion star is the main spectral feature in their spectra, while the ionized iron emission lines usually come from an accretion disk. The known NS HMXRBs in our sample – 4XMM J172511.3–361657 and 4XMM J174906.8–273233 – show no 6.7 keV emission, with upper limits on their equivalent widths (EWs) of 8 eV and 15 eV, respectively. We define the following criteria for the characterization of the NS HMXRB: (i) $P_{\text{spin}} \lesssim 1000$ s, (ii) $\text{HR} > -0.2$, (iii) $\text{EW}_{6.7} < 50$ eV, and (iv) a typical X-ray luminosity of $10^{33} - 10^{37}$ erg s $^{-1}$.

4.1.2. IPs

One of the prominent features of IPs is the presence of strong ionized 6.7 keV line emission. In our sample, all the confirmed IPs have a clear detection of a 6.7 keV line, with the lowest EW of the sample being 78_{-19}^{+34} for 4XMM J174517.0–321358. Xu et al. (2016) studied a sample of bright 17 IPs using *Suzaku* data. They found that the minimum and mean EW of the 6.7 keV line of the sample is 58_{-13}^{+10} and 107 ± 17 eV, respectively. The below criteria can be used to characterize IPs. They typically have (i) a spin period $P_{\text{spin}} < 2500$ s, (ii) an $\text{HR} > -0.2$, (iii) a strong 6.7 keV line emission with $\text{EW}_{6.7} > 50$ eV, and (iv) an X-ray luminosity in the range $10^{31} - 10^{35}$ erg s $^{-1}$ (Suleimanov et al. 2022).

4.1.3. Polars

The X-ray emission from polars is much softer than that of IPs. The spectra of many polars are dominated by very soft blackbody-like emission from the WD surface (Osborne et al. 1986; Ramsay et al. 1993; Clayton & Osborne 1994). However, toward the GC this component is difficult to observe due to the high absorption. In general polars also show a strong 6.7 keV line with an EW anywhere from 50 eV to ~ 450 eV (Ezuka & Ishida 1999; Xu et al. 2016). As a whole, the detection of a 6.7 keV line in polar can be difficult for faint sources as they are much softer than IPs. Polars can be tentatively classified by having softer spectra and periods above 2500 s; however, a secure classification would require the detection of the 6.7 keV line with good quality X-ray spectra and strong circular polarization in the optical band. The polars can be characterized by the following characteristics: (i) $P_{\text{spin}} = P_{\text{orb}} > 2500$ s, (ii) $\text{HR} < -0.2$, (iii) a strong 6.7 keV line emission with $\text{EW}_{6.7} > 50$ eV, and (iv) an X-ray luminosity below 10^{33} erg s $^{-1}$ (Suleimanov et al. 2022).

4.2. Known NS HMXRBs

The source 4XMM J172511.3–361657 was discovered on 9 February 2004 by INTEGRAL and named as IGR J17252–3616

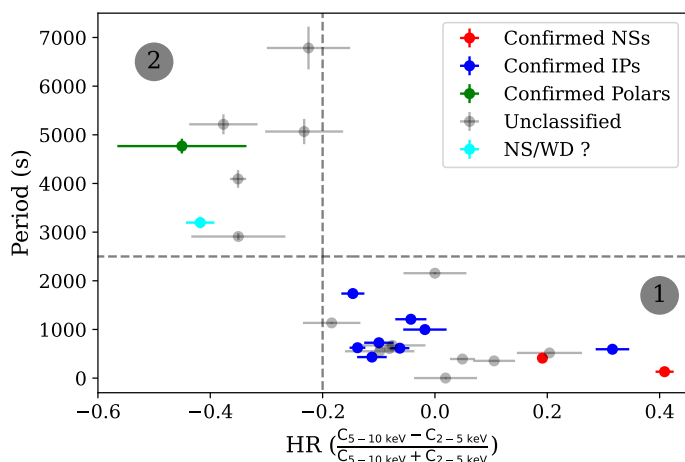


Fig. 6: HR vs. period diagram. The HR is calculated using the net counts of two bands: 2–5 keV and 5–10 keV.

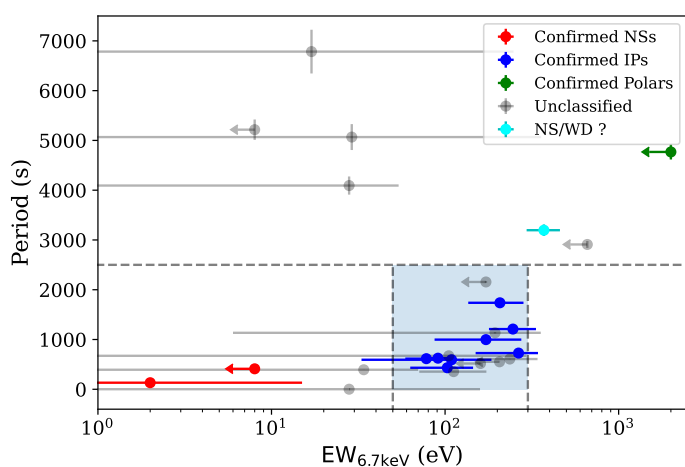


Fig. 7: EW of the 6.7 keV line vs. period diagram.

(Walter et al. 2004). *XMM-Newton* observed the source on 21 March 2004. A period search was performed by Zurita Heras et al. (2006), and a pulsation of 414.8 ± 0.5 s was discovered. An orbital period of 9.737 ± 0.004 days was also reported by using the Rossi X-ray Timing Explorer (RXTE) proportional counter array data (Markwardt & Swank 2003; Corbet et al. 2005). The source has a flat spectrum with $\Gamma = 0.82^{+0.04}_{-0.04}$, which can also be fitted by a flat power law with an energy cutoff or a Comptonized model with $kT \sim 5.5$ keV (Zurita Heras et al. 2006). The spectrum shows a 6.4 keV iron line with an EW of 70^{+6}_{-7} eV. Previous studies indicate the source is a wind-fed accreting pulsar with a supergiant companion star. The source has been observed multiple times by *XMM-Newton*, and we searched for pulsation in all the observations. The pulsations found in the different observations are consistent with each other within the 1σ error values. The source is highly variable, and the flux of the source can vary from 2.19×10^{-13} to 7.42×10^{-11} erg s $^{-1}$ cm $^{-2}$. We noticed that whenever the source flux drops below $\sim 5 \times 10^{-13}$ erg s $^{-1}$ cm $^{-2}$ the pulsation was undetectable.

The source 4XMM J174906.8–273233 was discovered in 1996 by ASCA. The source is also known as AXJ1749.1–2733 (Sakano et al. 2002). In a 1995 ASCA observation, the source was not detected, and in 2003 INTEGRAL caught a short outburst, which indicates its transient nature (Grebenev et al. 2004). *XMM-Newton* first observed 4XMM J174906.8–273233 on 31

March 2007, and Karasev et al. (2008) analyzed EPIC-pn data and detected a spin period of 132 s. The source was classified as a transient X-ray pulsar in a high-mass binary system. The source has been observed twice by *XMM-Newton* in 2007 and 2008; however, the pulsation was only detected in the 2007 observation (ObsID: 0510010401). The non-detection of pulsations in 2008 could be due to the combination of two factors: (1) the source flux was almost an order of magnitude fainter than in the 2007 observation, and (2) the 2008 observation had a shorter exposure than the 2007 observation, which led to ~ 22 times fewer net counts in the 2008 observation than in the 2007 observation. The source spectrum is heavily absorbed and can be fitted by a steep power-law model with $\Gamma = 1.3^{+0.1}_{-0.1}$; adding an iron line at 6.4 keV improves the fit minutely.

4.3. Known IPs

The source 4XMM J174517.0–321358 (Gong 2022; Vermette et al. 2023) was discovered by *Chandra* and serendipitously observed by *XMM-Newton* in 2010. An iron-line emission complex and a pulsation of 614 s were detected using *XMM-Newton* data. The source is classified as an IP with a WD of $0.8M_{\odot}$ (Vermette et al. 2023). The source has been observed twice by *XMM-Newton*, and in both observations, we detected a pulsation of 613 s. The X-ray spectrum looks like that of a typical IP with a flat spectral shape and iron emission complex.

The source 4XMM J174033.8–301501 was discovered by *Suzaku* in 2008 (Uchiyama et al. 2011a). Later, the source was observed by *XMM-Newton* on 18 March 2021 during a Galactic disk survey (Mondal et al. 2022). The source spectrum is well described by emission from collisionally ionized diffuse gas with a plasma temperature of ~ 15.7 keV plus an iron line emission complex. A period of 432.4 s was detected in both *Suzaku* and *XMM-Newton* data. The source has been observed twice by *XMM-Newton* in 2018 and 2021. In both *XMM-Newton* observations, the detected pulsations are consistent. The source has a flat spectrum with $\Gamma = 0.5^{+0.1}_{-0.1}$ and an Fe emission complex in the 6–7 keV band.

4XMM J174954.6–294336 was first discovered by *Chandra* (Jonker et al. 2014). The source is classified as an IP based on the spin period of 1002 s and hard power-law spectral shape with complex iron line emission (Johnson et al. 2017; Mondal et al. 2023). This is only the second known IP that shows eclipses in X-rays. The source has been observed twice by *XMM-Newton*, and the pulsation is not visible in ObsID 0801681401. Mondal et al. (2023) discuss the possibility that the pulsation is suppressed due to a complex absorption behavior and the eclipse seen in the X-ray light curve.

4XMM J174917.7–283329 is classified as IP (Mondal et al. 2023). A period of 1212 s was detected in a 2017 *XMM-Newton* observation. The continuum is best fitted by a partially absorbed apec model with a plasma temperature of 13 keV. The source has been observed three times by *XMM-Newton*, but the pulsation was detected only once, when the source flux was one order of magnitude higher than in the other two observations.

The source 4XMM J174816.9–280750 was observed by BeppoSAX during the GC survey in 1997–1998 (Sidoli et al. 2006). The source has a spectrum with $\Gamma = 1.3^{+0.6}_{-0.6}$ and strong emission lines at 6–7 keV, plus a coherent pulsation of period 593 s was found in *Suzaku* and *XMM-Newton* data. These facts favor the source as an IP (Nobukawa et al. 2009). The source has been observed ten times by *XMM-Newton*, displaying significant variation in the pulsation period between different observations. A detailed, in-depth study of the source is required to determine

whether the pulsation period variation is due to accretion or some other effects, such as the propeller phenomenon.

4XMM J174016.0–290337 was observed by *XMM-Newton* on 29 September 2005 (Farrell et al. 2010). The source displays Fe K_{α} emission and a periodic modulation with a period of 626 s. The source has been observed three times by *XMM-Newton*, and in all cases, a pulsation period of 622 s is detected.

The source 4XMM J174009.0–28472 was first discovered by ASCA (Sakano et al. 2000) and a period of 729 s was found. The source was classified as NS pulsar based on the flat power-law-type spectrum shape (Sakano et al. 2000). However, later near-infrared/optical studies suggested it is an IP (Kaur et al. 2010). The source has been observed four times by *XMM-Newton*, and we detected a similar pulsation period value in all observations. The source has a very flat spectrum $\Gamma = 0.1^{+0.1}_{-0.1}$ with strong emission lines.

4XMM J174622.7–285218 is classified as an IP (Nucita et al. 2022). The source was first observed in a *Chandra* observation of the GC, and a periodic signal of 1745 s was found (Muno et al. 2009). The spectrum is characterized by $\Gamma = 0.7^{+0.2}_{-0.2}$, and the 6.9 keV line is the strongest with an EW of 242^{+81}_{-74} .

4.4. Known polars

The source 4XMM J174728.9–321441 was first observed by *Chandra* during the Galactic bulge survey (Jonker et al. 2014). The source is classified as a polar based on its long period of 4860 s detected in X-rays and in He II $\lambda 5412$ line emission (Wevers et al. 2017). This source has the steepest spectrum in our sample with $\Gamma = 1.8^{+0.4}_{-0.4}$, and no iron emission complex was detected in the *XMM-Newton* spectrum. The non-detection of iron lines could be due to low signal-to-noise in the data.

4.5. Unclassified sources

Below, we try to classify the unknown sources using the scheme defined in Sect. 4.1. This is a tentative classification; further follow-up of the individual sources is required to constrain their true nature. For many sources, we do not have any *Gaia* counterpart; therefore, the estimation of the distance to the source using parallax was not possible and hence the luminosity is not calculated. In such a case, we only used the first three criteria for classification.

4.5.1. Likely NS HMXRBs

The only two sources matching the NS HMXRB criteria are XMMU J175441.9–265919 and 4XMM J175525.0–260402. Both have relatively high HR values: 0.02 ± 0.06 and 0.05 ± 0.02 , respectively. The upper limits on the EWs of the 6.7 keV line for J175441.9 and J175525.0 are ~ 28 eV and ~ 34 eV, respectively. The spin periods of these two systems are 1.36 s and 392.5 s. The source J175525.0 was detected three times by *XMM-Newton*; however, the pulsation was detected only in the longest observation. A luminosity estimation was not possible as we did not find any counterparts in *Gaia* catalogs.

4.5.2. Likely IPs

The sources we categorize as IP are 4XMM J173058.9–350812, 4XMM J175301.3–291324, 4XMM J175740.5–285105, and 4XMM J175511.6–260315. The periods found from these systems are below 2500 s and the HRs are above -0.2. The 6.7 keV

line EWs for the sources J173058.9, J175301.3, J175740.5, and J175511.6 are 236^{+105}_{-83} , 105^{+189} , 112^{+61}_{-41} , and 194^{+162}_{-188} eV, respectively. The source J175301.3 was observed three times by *XMM-Newton*, and a ~ 672 s period was consistently found in two of those observations. The source J175511.6 was detected three times by *XMM-Newton*; however, the period of ~ 1135 s was detected only in the longest observation. We detected a likely *Gaia* counterpart for the sources J173058.9 and J175511.6 and the distances estimated from their parallaxes are $3.2^{+2.2}_{-1.3}$ and $4.9^{+3.2}_{-2.4}$ kpc, respectively. The luminosity of these two sources is in the range $(0.8 - 1.9) \times 10^{33}$ erg s $^{-1}$, which is typical for accreting magnetic CVs (Suleimanov et al. 2022).

4.5.3. Likely polars

The sources that are likely to be polars are 4XMM J173837.0–304818, 4XMM J175327.8–295716, 4XMM J175244.4–285851, 4XMM J175328.4–244627, and XMMU J180140.3–234221. These sources have very low HR values and long periods (see Fig. 6), which suggests that these sources are most likely to be polars. The long periods are most likely associated with the synchronized spin-orbital period of the WDs. All these sources have relatively soft spectra of photon index $\Gamma = 0.8 - 2.1$. For most of the polar-type sources, we have an upper limit on the EW of the 6.7 keV emission line. This is primarily because these sources have very low net counts that give ≤ 50 bins in the 0.2–10 keV spectrum. The source J175328.4 is the brightest in the polar sample and has the best signal-to-noise spectrum compared to the other four sources. In this case, the EW of the 6.7 keV emission line is 28^{+26}_{-28} eV, which is much smaller than the typical values found in IPs. The source J175327.8 was observed six times by *XMM-Newton*; however, the periodicity was significantly detected only in the two observations that have an exposure above 25 ks. We found a likely *Gaia* counterpart for the source J175328.4 and its estimated distance is $1.8^{+0.4}_{-0.2}$ kpc, giving a luminosity of 2×10^{33} erg s $^{-1}$.

4.5.4. Unknowns

We classify the sources XMMU J173029.8–330920, 4XMM J174809.8–300616, and 4XMM J175452.0–295758 as unknowns. These sources have high HR and periods similar to IPs. However, the 6.7 keV line was not detected clearly and we could only set an upper limit on its EW. The EW of the 6.7 keV line for the sources J173029.8, J174809.8, and J175452.0 are <160 , <172 , and <206 eV, respectively. The source J174809.8 has been observed twice by *XMM-Newton*. However, it is relatively faint, with a flux of a few times 10^{-13} erg cm $^{-2}$ s $^{-1}$ and therefore the period was detected only in the longer observation. The source J175452.0 was detected three times by *XMM-Newton*; however, the pulsation was detected only in the longest observation.

4.5.5. NS or WD?

The compact object in 4XMM J174445.6–271344 is not clearly identified. Also known as HD 161103, it was observed by *XMM-Newton* on 26 January 2004. Lopes de Oliveira et al. (2006) did a detailed multiwavelength spectroscopic study of this source and suggested that the system hosts an NS; however, a WD scenario was not excluded. From optical spectroscopy, the companion star of this system is recognized as a Be star. We detected a periodicity of 3196 s from the X-ray light curve. The X-ray spectra show strong 6.4, 6.7, and 6.9 keV emission lines

Table 1: Sources with possible *Gaia* optical counterparts.

XMM Name	Density arcsec ⁻²	G_{mag}	Plx mas	Distance kpc	L_x erg s ⁻¹
4XMM J173058.9	0.009	20.05	0.59	$3.2^{+2.2}_{-1.3}$	1.9×10^{33}
4XMM J174033.8	0.009	19.23	0.23	$4.3^{+1.5}_{-1.3}$	6.4×10^{33}
4XMM J174009.0	0.03	18.79	0.71	$1.8^{+1.2}_{-0.5}$	2.3×10^{33}
4XMM J174954.6	0.1	18.97	0.61	$1.6^{+2.8}_{-2.5}$	5.3×10^{32}
4XMM J174816.9	0.01	21.13	0.63	$2.9^{+2.3}_{-1.4}$	8.6×10^{32}
4XMM J175511.6	0.02	18.64	0.40	$4.9^{+3.2}_{-2.4}$	8.8×10^{32}
4XMM J175328.4	0.02	8.40	0.55	$1.8^{+0.4}_{-0.2}$	2.2×10^{33}

Notes. Sources with *Gaia* counterparts found within the 3σ positional error of *XMM-Newton*. The density was calculated by drawing a circle with a radius of 1 arcmin at the source position.

with EWs of 80^{+39}_{-40} , 371^{+88}_{-76} , and 109^{+43}_{-47} eV, respectively. Such strong 6.7 and 6.9 keV emission lines are not typically seen in accreting NS HMXRBs. Also, the source has a much softer spectrum (HR = -0.42 ± 0.03 in Fig. 6) than the two confirmed NS HMXRBs (4XMM J172511.3–361657 and 4XMM J172511.3–361657) in our sample.

5. Conclusion

We systematically searched for periodic X-ray sources in the inner Galactic disk, which extends from $l \sim 350^\circ$ to $l \sim +7^\circ$ and includes the GC, using *XMM-Newton* Heritage observations and archival data. We find 26 sources that show periodicity in their X-ray light curves, of which 12 have previously reported periods. For these 12 sources, we have obtained periods consistent with those previously reported. We have detected the periodicity in the other 14 sources for the first time. We classified the sources based on the values of the HR, period, and iron emission complex in the 6–7 keV band. Of these 14 sources, we classify two as NS X-ray binaries, four as likely IPs, five as likely polars, and three as unknowns. The IP-type sources display a steep X-ray spectrum with $\Gamma \leq 1.1$ and an iron emission complex in the 6–7 keV band. The spectra of polars are much softer compared to IPs.

Acknowledgements. SM and GP acknowledge financial support from the European Research Council (ERC) under the European Union’s Horizon 2020 research and innovation program HotMilk (grant agreement No. 865637). SM and GP also acknowledge support from Bando per il Finanziamento della Ricerca Fondamentale 2022 dell’Istituto Nazionale di Astrofisica (INAF): GO Large program and from the Framework per l’Attrazione e il Rafforzamento delle Eccellenze (FARE) per la ricerca in Italia (R20L5S39T9). KM is partially supported by the NASA ADAP program (NNH22ZDA001N-ADAP). We thank the referee for the comments, corrections, and suggestions that significantly improved the manuscript.

References

Aizu, K. 1973, *Progress of Theoretical Physics*, 49, 1184
Anastasopoulou, K., Ponti, G., Sormani, M. C., et al. 2023, *A&A*, 671, A55
Arnaud, K. A. 1996, in *Astronomical Society of the Pacific Conference Series*, Vol. 101, *Astronomical Data Analysis Software and Systems V*, ed. G. H. Jacoby & J. Barnes, 17
Ashley, R. P., Marsh, T. R., Breedt, E., et al. 2020, *MNRAS*, 499, 149
Astropy Collaboration, Price-Whelan, A. M., Lim, P. L., et al. 2022, *ApJ*, 935, 167

Astropy Collaboration, Price-Whelan, A. M., Sipőcz, B. M., et al. 2018, *AJ*, 156, 123
Astropy Collaboration, Robitaille, T. P., Tollerud, E. J., et al. 2013, *A&A*, 558, A33
Bahramian, A., Heinke, C. O., Kennea, J. A., et al. 2021, *MNRAS*, 501, 2790
Bailer-Jones, C. A. L., Rybizki, J., Fouvésneau, M., Demleitner, M., & Andrae, R. 2021, *AJ*, 161, 147
Baluev, R. V. 2008, *MNRAS*, 385, 1279
Bao, T. & Li, Z. 2022, *MNRAS*, 509, 3504
Clayton, K. L. & Osborne, J. P. 1994, *MNRAS*, 268, 229
Corbet, R. H. D., Markwardt, C. B., & Swank, J. H. 2005, *ApJ*, 633, 377
Cropper, M. 1990, *Space Sci. Rev.*, 54, 195
Downes, R. A., Webbink, R. F., Shara, M. M., et al. 2001, *PASP*, 113, 764
Ezuka, H. & Ishida, M. 1999, *ApJS*, 120, 277
Farrell, S. A., Gosling, A. J., Webb, N. A., et al. 2010, *A&A*, 523, A50
Foreman-Mackey, D., Hogg, D. W., Lang, D., & Goodman, J. 2013, *PASP*, 125, 306
Gong, H. 2022, *ApJ*, 933, 240
Grebenev, S. A., Rodriguez, J., Westergaard, N. J., Sunyaev, R. A., & Oosterbroek, T. 2004, *The Astronomer’s Telegram*, 252, 1
Haberl, F. & Motch, C. 1995, *A&A*, 297, L37
Hailey, C. J., Mori, K., Perez, K., et al. 2016, *ApJ*, 826, 160
Hofmann, F., Ponti, G., Haberl, F., & Clavel, M. 2018, *A&A*, 615, L7
Jansen, F., Lumb, D., Altieri, B., et al. 2001, *A&A*, 365, L1
Johnson, C. B., Torres, M. A. P., Hynes, R. I., et al. 2017, *MNRAS*, 466, 129
Jonker, P. G., Torres, M. A. P., Hynes, R. I., et al. 2014, *ApJS*, 210, 18
Karasev, D. I., Tsygankov, S. S., & Lutovinov, A. A. 2008, *MNRAS*, 386, L10
Kaur, R., Wijnands, R., Paul, B., Patruno, A., & Degenaar, N. 2010, *MNRAS*, 402, 2388
Lomb, N. R. 1976, *Ap&SS*, 39, 447
Lopes de Oliveira, R., Bruch, A., Rodrigues, C. V., Oliveira, A. S., & Mukai, K. 2020, *ApJ*, 898, L40
Lopes de Oliveira, R., Motch, C., Haberl, F., Negueruela, I., & Janot-Pacheco, E. 2006, *A&A*, 454, 265
Markwardt, C. B. & Swank, J. H. 2003, *The Astronomer’s Telegram*, 179, 1
Mondal, S., Ponti, G., Haberl, F., et al. 2022, *A&A*, 666, A150
Mondal, S., Ponti, G., Haberl, F., et al. 2023, *A&A*, 671, A120
Mukai, K. 2017, *PASP*, 129, 062001
Muno, M. P., Arabadjis, J. S., Baganoff, F. K., et al. 2004, *ApJ*, 613, 1179
Muno, M. P., Baganoff, F. K., Bautz, M. W., et al. 2003a, *ApJ*, 589, 225
Muno, M. P., Baganoff, F. K., Bautz, M. W., et al. 2003b, *ApJ*, 599, 465
Muno, M. P., Bauer, F. E., Baganoff, F. K., et al. 2009, *ApJS*, 181, 110
Neumann, M., Avakyan, A., Doroshenko, V., & Santangelo, A. 2023, *A&A*, 677, A134
Nishiyama, S., Yasui, K., Nagata, T., et al. 2013, *ApJ*, 769, L28
Nobukawa, M., Koyama, K., Matsumoto, H., & Tsuru, T. G. 2009, *PASJ*, 61, S93
Norton, A. J. & Watson, M. G. 1989, *MNRAS*, 237, 853
Nucita, A. A., Lezzi, S. M., De Paolis, F., et al. 2022, *MNRAS*, 517, 118
Osborne, J. P., Bonnet-Bidaud, J. M., Bowyer, S., et al. 1986, *MNRAS*, 221, 823
Patterson, J. 1994, *PASP*, 106, 209
Perez, K., Hailey, C. J., Bauer, F. E., et al. 2015, *Nature*, 520, 646
Ponti, G., Hofmann, F., Churazov, E., et al. 2019, *Nature*, 567, 347
Ponti, G., Morris, M. R., Churazov, E., Heywood, I., & Fender, R. P. 2021, *A&A*, 646, A66
Ponti, G., Morris, M. R., Terrier, R., & Goldwurm, A. 2013, in *Astrophysics and Space Science Proceedings*, Vol. 34, *Cosmic Rays in Star-Forming Environments*, ed. D. F. Torres & O. Reimer, 331
Ponti, G., Morris, M. R., Terrier, R., et al. 2015, *MNRAS*, 453, 172
Predehl, P., Sunyaev, R. A., Becker, W., et al. 2020, *Nature*, 588, 227
Ramsay, G., Rosen, S. R., Mason, K. O., Cropper, M. S., & Watson, M. G. 1993, *MNRAS*, 262, 993
Revnitvsev, M., Sazonov, S., Churazov, E., et al. 2009, *Nature*, 458, 1142
Ritter, H. & Kolb, U. 2003, *A&A*, 404, 301
Sakano, M., Koyama, K., Murakami, H., Maeda, Y., & Yamauchi, S. 2002, *ApJS*, 138, 19
Sakano, M., Torii, K., Koyama, K., Maeda, Y., & Yamauchi, S. 2000, *PASJ*, 52, 1141
Saxton, C. J., Wu, K., Cropper, M., & Ramsay, G. 2005, *MNRAS*, 360, 1091
Scargle, J. D. 1982, *ApJ*, 263, 835
Scaringi, S., Bird, A. J., Norton, A. J., et al. 2010, *MNRAS*, 401, 2207
Sidoli, L., Mereghetti, S., Favata, F., Oosterbroek, T., & Parmar, A. N. 2006, *A&A*, 456, 287
Strüder, L., Briel, U., Dennerl, K., et al. 2001, *A&A*, 365, L18
Su, M., Slatyer, T. R., & Finkbeiner, D. P. 2010, *ApJ*, 724, 1044
Suleimanov, V. F., Doroshenko, V., & Werner, K. 2022, *MNRAS*, 511, 4937
Timmer, J. & Koenig, M. 1995, *A&A*, 300, 707
Turner, M. J. L., Abbey, A., Arnaud, M., et al. 2001, *A&A*, 365, L27
Uchiyama, H., Koyama, K., Matsumoto, H., et al. 2011a, *PASJ*, 63, S865

- Uchiyama, H., Nobukawa, M., Tsuru, T., Koyama, K., & Matsumoto, H. 2011b, *PASJ*, **63**, S903
- Vaughan, S. 2010, *MNRAS*, **402**, 307
- Vaughan, S., Edelson, R., Warwick, R. S., & Uttley, P. 2003, *MNRAS*, **345**, 1271
- Verbunt, F., Bunk, W. H., Ritter, H., & Pfeffermann, E. 1997, *A&A*, **327**, 602
- Vermette, B., Salcedo, C., Mori, K., et al. 2023, *ApJ*, **954**, 138
- Walter, R., Bodaghee, A., Barlow, E. J., et al. 2004, *The Astronomer's Telegram*, **229**, 1
- Wang, Q. D., Gotthelf, E. V., & Lang, C. C. 2002, *Nature*, **415**, 148
- Warner, B. 1989, *Information Bulletin on Variable Stars*, **3383**, 1
- Warner, B. 2003, *Cataclysmic Variable Stars*
- Warwick, R. S., Turner, M. J. L., Watson, M. G., & Willingale, R. 1985, *Nature*, **317**, 218
- Webb, N. A., Coriat, M., Traulsen, I., et al. 2020, *A&A*, **641**, A136
- Wevers, T., Torres, M. A. P., Jonker, P. G., et al. 2017, *MNRAS*, **470**, 4512
- Wilms, J., Allen, A., & McCray, R. 2000, *ApJ*, **542**, 914
- Worrall, D. M., Marshall, F. E., Boldt, E. A., & Swank, J. H. 1982, *ApJ*, **255**, 111
- Xu, X.-j., Wang, Q. D., & Li, X.-D. 2016, *ApJ*, **818**, 136
- Yamauchi, S., Kaneda, H., Koyama, K., et al. 1996, *PASJ*, **48**, L15
- Yasui, K., Nishiyama, S., Yoshikawa, T., et al. 2015, *PASJ*, **67**, 123
- Zhu, Z., Li, Z., & Morris, M. R. 2018, *ApJS*, **235**, 26
- Zurita Heras, J. A., De Cesare, G., Walter, R., et al. 2006, *A&A*, **448**, 261

Appendix A: Additional figures and tables

Table A.1: Various details of the X-ray pulsators in the GC plus Galactic disk.

lat	lon	ObsID	Pos _{err} arcsec	Period (s)		PF 2–10 keV	XMM Name	P _{Gaia}	Sig > σ	Type	References
				Otr	Previous						
351.4972	-0.3537	0886070601	0.14	414.5 ± 1.4	414.8	68.4 ± 1.6	4XMM J172511.3–361657	4 × 10 ⁻⁴	3	NS HMXRB	Zurita Heras et al. (2006)
353.1032	-0.6956	0861171201	0.73	607.5 ± 3.7		45.6 ± 10.8	4XMM J173058.9–350812	1.5 × 10 ⁻²	3	Likely IP	
354.7018	0.4782	0916800201	0.35	517.6 ± 3.6		41.3 ± 12.5	XMMU J173029.8–330920	1 × 10 ⁻³	3	Unknown	Mondal et al. in prep
357.1486	-1.6563	0865510101	0.48	614.2 ± 1.4	614	28.2 ± 4.5	4XMM J174517.0–321358	4 × 10 ⁻³	3	IP	Vermette et al. (2023)
357.3792	-2.0600	0743980401	0.57	4768.3 ± 151.5	4860	74.2 ± 22.4	4XMM J174728.9–321441	2.1 × 10 ⁻²	3	Polar	Wevers et al. (2017)
357.6116	0.3037	0886020101	0.79	5067.3 ± 260.5		57.9 ± 16.2	4XMM J173837.0–304818	1.2 × 10 ⁻²	3	Likely Polar	
358.3043	0.2442	0886010601	0.48	432.4 ± 1.9	432.1	54.8 ± 7.7	4XMM J174033.8–301501	6.8 × 10 ⁻³	3	IP	Mondal et al. (2022)
359.2786	0.9300	0764191201	0.17	623.2 ± 2.6	626	37.2 ± 3.8	4XMM J174016.0–290337	1.4 × 10 ⁻³	3	IP	Farrell et al. (2010)
359.2882	-1.0793	0152920101	0.65	2179.6 ± 18.2		64.1 ± 19	4XMM J174809.8–300616	2.5 × 10 ⁻²	3	Unknown	
359.4941	1.0946	0764191101	0.6	725.9 ± 3.5	729	45.1 ± 6.8	4XMM J174009.0–284725	3.2 × 10 ⁻²	3	IP	Kaur et al. (2010)
359.8061	-1.2096	0801683401	0.56	997.7 ± 7.6	1001.5	31 ± 8.9	4XMM J174954.6–294336	7.7 × 10 ⁻²	3	IP	Mondal et al. (2023)
0.0036	-1.9883	0801682901	0.76	2917.0 ± 68.5		54.9 ± 12.7	4XMM J175327.8–295716	1.8 × 10 ⁻¹	2	Likely Polar	
0.1413	-0.1089	0762250301	0.32	1737.7 ± 5.4	1745	15.8 ± 3.7	4XMM J174622.7–285218	2.5 × 10 ⁻³	2	IP	Muno et al. (2009)
0.1476	-2.2564	0402280101	0.59	552.1 ± 1.4		45.1 ± 9.8	4XMM J175452.0–295758	9.9 × 10 ⁻²	3	Unknown	
0.5849	-1.5353	0801682801	0.49	672.5 ± 3.0		77.8 ± 18.9	4XMM J175301.3–291324	7.7 × 10 ⁻²	3	Likely IP	
0.7407	-0.4932	0801681301	0.44	1209.7 ± 11.7	1212.4	44.3 ± 8.3	4XMM J174917.7–283329	1.3 × 10 ⁻²	3	IP	Mondal et al. (2023)
0.7632	-1.3587	0801682601	0.97	6784.4 ± 439.5		73 ± 20.4	4XMM J175244.4–285851	2.8 × 10 ⁻¹	3	Likely Polar	Bahramian et al. (2021)
0.9918	-0.0821	0783160101	0.47	593.6 ± 0.7	593	41.3 ± 7.3	4XMM J174816.9–280750	6.8 × 10 ⁻²	3	IP	Sidoli et al. (2006)
1.3573	1.0522	0201200101	1.9	3195.8 ± 116.3	3200	28.9 ± 6.5	4XMM J174445.6–271344	6.2 × 10 ⁻¹	3	NS/WD ?	Lopes de Oliveira et al. (2006)
1.4196	-2.2266	0782270201	0.51	354.68 ± 0.7		47.6 ± 10.9	4XMM J175740.5–285105	9.2 × 10 ⁻¹	3	Likely IP	
1.5909	0.0633	0510010401	1.9	132.1 ± 0.3	132	28.9 ± 3.4	4XMM J174906.8–273233	2.0 × 10 ⁻¹	3	NS HMXRB	Karasev et al. (2008)
2.6999	-0.7212	0886081101	0.59	1.36652 ± 2 × 10 ⁻⁵		48.1 ± 12.6	XMMU J175441.9–265919	7.7 × 10 ⁻³	3	Likely NS XRB	
3.5626	-0.3453	0886081301	0.53	1134.5 ± 12.4		79.1 ± 14.4	4XMM J175511.6–260315	1.7 × 10 ⁻²	3	Likely IP	
3.5766	-0.3953	0886081301	0.51	392.5 ± 1.5		28.2 ± 5	4XMM J175525.0–260402	1.5 × 10 ⁻²	3	Likely NS XRB	
4.4701	0.6376	0840910501	0.36	4093.3 ± 182.3		34.8 ± 6.1	4XMM J175328.4–244627	8.8 × 10 ⁻²	3	Likely Polar	
6.3308	-0.4448	0886110501	0.64	5215.9 ± 7.5		61.8 ± 19.3	XMMU J180140.3–234221	1.7 × 10 ⁻²	2	Likely Polar	

Notes. The details of the X-ray pulsators, including the positional information, XMM-Newton detection ID, and the source association in the 4XMM catalog. The source XMMU J173029.8–330920, XMMU J175441.9–265919, and XMMU J180140.3–234221 are the first time detected by XMM-Newton in our ongoing *Heritage* survey of the Galactic disk. We also searched for *Swift*-XRT and *Chandra* counterparts of these two sources, but no counterparts were found. The P_{Gaia} represents the probability of spurious association with a *Gaia* source.

Table A.2: Details of the pulsators for which more than one observation is available.

XMM Name	ObsID	Date	Flux erg s ⁻¹ cm ⁻²	Period	Exposure ks
4XMM J172511.3–361657	0206380401	2004-03-21	$(7.42 \pm 0.04) \times 10^{-11}$	413.8 ± 3.7	10.9
	0405640201	2006-08-29	$(3.94 \pm 0.17) \times 10^{-13}$		22.9
	0405640301	2006-08-31	$(6.46 \pm 0.04) \times 10^{-11}$	414.5 ± 3.8	11.3
	0405640401	2006-09-04	$(2.55 \pm 0.02) \times 10^{-11}$	414.4 ± 3.3	12.5
	0405640501	2006-09-06	$(3.21 \pm 0.08) \times 10^{-12}$	409.8 ± 3.5	11.9
	0405640601	2006-09-08	$(5.53 \pm 0.27) \times 10^{-13}$		13.9
	0405640701	2006-09-15	$(1.81 \pm 0.02) \times 10^{-11}$	414.4 ± 1.7	22.9
	0405641001	2006-09-27	$(2.19 \pm 0.21) \times 10^{-13}$		12.4
	0405640901	2006-09-28	$(2.77 \pm 0.02) \times 10^{-11}$	413.9 ± 2.6	15.2
	0405640801	2006-10-01	$(4.12 \pm 0.02) \times 10^{-11}$	413.2 ± 2.5	15.7
	0886070601	2006-10-01	$(3.56 \pm 0.03) \times 10^{-11}$	414.5 ± 1.4	26.6
4XMM J174517.0–321358	0553950201	2010-10-09	$(2.10 \pm 0.06) \times 10^{-12}$	613.8 ± 0.9	86.4
	0870990201	2021-02-28	$(1.24 \pm 0.02) \times 10^{-12}$	614.2 ± 2.4	31.6
	0865510101	2021-03-02	$(1.26 \pm 0.02) \times 10^{-12}$	614.2 ± 1.4	62.9
4XMM J174033.8–301501	0823030101	2018-09-29	$(1.96 \pm 0.09) \times 10^{-12}$	433.0 ± 5.6	8.0
	0886010601	2021-03-18	$(2.88 \pm 0.06) \times 10^{-12}$	432.4 ± 1.9	23.0
4XMM J174016.0–290337	0304220101	2005-09-29	$(3.61 \pm 0.13) \times 10^{-12}$	624.8 ± 9.4	8.5
	0764191201	2016-03-05	$(5.14 \pm 0.06) \times 10^{-12}$	623.2 ± 2.6	33
	0764191101	2016-03-05	$(8.78 \pm 0.30) \times 10^{-12}$	622.6 ± 2.6	33
4XMM J174809.8–300616	0152920101	2003-04-02	$(2.96 \pm 0.17) \times 10^{-13}$	2179.6 ± 18.2	52.2
	0801683301	2018-04-06	$(2.08 \pm 0.39) \times 10^{-13}$		29.8
4XMM J174009.0–284725	0511010701	2008-02-27	$(3.75 \pm 0.09) \times 10^{-12}$	733.1 ± 14.6	9.3
	0764191501	2016-02-25	$(5.89 \pm 0.22) \times 10^{-12}$	725.5 ± 3.7	30.5
	0764191101	2016-03-05	$(5.90 \pm 0.14) \times 10^{-12}$	725.9 ± 3.5	33
	0764191601	2016-03-10	$(5.63 \pm 0.21) \times 10^{-12}$	725.5 ± 6.0	19
4XMM J174954.6–294336	0801681401	2017-10-07	$(1.28 \pm 0.05) \times 10^{-12}$		28
	0801683401	2018-04-06	$(1.73 \pm 0.06) \times 10^{-12}$	997.7 ± 7.6	29.2
4XMM J175327.8–295716	0085580501	2000-10-11	$(3.35 \pm 0.48) \times 10^{-13}$		8.0
	0085581501	2001-03-24	$(1.93 \pm 1.22) \times 10^{-13}$		7.5
	0085581601	2001-09-07	$(3.77 \pm 1.07) \times 10^{-13}$		8.2
	0085581801	2002-03-13	$(1.21 \pm 0.53) \times 10^{-13}$		8.2
	0801682901	2018-09-07	$(4.29 \pm 0.38) \times 10^{-13}$	2917.0 ± 68.5	27.9
	0801683601	2018-09-25	$(3.05 \pm 0.31) \times 10^{-13}$	2870.2 ± 58.1	31.7
4XMM J175452.0–295758	0085580501	2000-10-11	$(1.88 \pm 0.45) \times 10^{-13}$		8.0
	0206590201	2004-09-05	$(2.46 \pm 0.27) \times 10^{-13}$		20.9
	0402280101	2006-09-10	$(2.68 \pm 0.19) \times 10^{-13}$	552.1 ± 1.4	44.1
4XMM J175301.3–291324	0801682501	2018-09-03	$(3.29 \pm 1.29) \times 10^{-13}$		29.0
	0801682801	2018-09-09	$(1.86 \pm 0.11) \times 10^{-13}$	673.1 ± 3.1	32.9
	0801683501	2018-09-25	$(4.12 \pm 0.57) \times 10^{-13}$	672.5 ± 3.0	31.5

Notes. The *XMM-Newton* ObsIDs details for sources in which more than one observation is available. The flux is taken from the 4XMM catalog. In many cases, the pulsation was not detected if the exposure was short or the source flux was below a certain limit.

Table A.3: Table A.2 Continued.

XMM Name	ObsID	Date	Flux	Period	Exposure
4XMM J174917.7–283329	0410580401	2006-09-22	$(1.85 \pm 0.50) \times 10^{-13}$		32.9
	0410580501	2006-09-26	$(3.07 \pm 0.63) \times 10^{-13}$		32.4
	0801681301	2017-10-07	$(1.32 \pm 0.03) \times 10^{-12}$	1209.7 ± 11.7	28.0
4XMM J174816.9–280750	0112970101	2000-09-23	$(7.89 \pm 0.43) \times 10^{-13}$	595.1 ± 5.5	16.3
	0112970201	2000-09-23	$(9.34 \pm 0.79) \times 10^{-13}$	587.8 ± 4.5	18.1
	0144220101	2003-03-12	$(9.42 \pm 0.61) \times 10^{-13}$	592.9 ± 1.4	52.4
	0205240101	2005-02-26	$(6.37 \pm 0.19) \times 10^{-13}$	592.7 ± 1.4	51
	0694640801	2012-10-06	$(8.04 \pm 0.37) \times 10^{-13}$	590.9 ± 1.7	41.9
	0694641501	2012-10-06	$(6.67 \pm 0.17) \times 10^{-13}$	592.9 ± 1.4	51.8
	0694640701	2012-10-02	$(6.47 \pm 0.19) \times 10^{-13}$	592.5 ± 1.7	44.4
	0694641401	2012-09-30	$(7.43 \pm 0.41) \times 10^{-13}$		51.8
	0783160101	2016-10-02	$(8.51 \pm 0.23) \times 10^{-13}$	593.6 ± 0.7	106
	0862471201	2020-10-04	$(1.01 \pm 0.05) \times 10^{-12}$		46.9
4XMM J174445.6–271344	0201200101	2004-02-26	$(2.03 \pm 0.04) \times 10^{-12}$	3195.8 ± 116.3	17.8
	0691760101	2012-09-08	$(1.33 \pm 0.02) \times 10^{-12}$		22.9
4XMM J174906.8–273233	0510010401	2007-03-31	$(1.13 \pm 0.01) \times 10^{-11}$	132.1 ± 0.3	12.2
	0511010301	2008-03-04	$(2.44 \pm 0.12) \times 10^{-12}$		8.9
4XMM J175511.6–260315	0148090101	2003-03-17	$(1.07 \pm 0.14) \times 10^{-12}$		12.1
	0148090501	2003-09-11	$(1.53 \pm 0.17) \times 10^{-12}$		11.2
	0886081301	2023-04-06	$(3.06 \pm 0.21) \times 10^{-12}$	1134.5 ± 12.4	24
4XMM J175525.0–260402	0148090101	2003-03-17	$(3.03 \pm 0.30) \times 10^{-12}$		12.1
	0148090501	2003-09-11	$(4.47 \pm 0.43) \times 10^{-12}$		11.2
	0886081301	2023-04-06	$(1.84 \pm 0.10) \times 10^{-12}$	392.5 ± 1.5	24

Notes. Same columns as Table A.2.

Table A.4: Details of the spectral fit.

XMM Name	N_{H} $\times 10^{22} \text{ cm}^{-2}$	Γ	N_{po}	$N_{6.4}$	EW _{6.4} eV	$N_{6.7}$	EW _{6.7} eV	$N_{6.9}$	EW _{6.9} eV	$\chi^2/\text{d.o.f}$	Flux 0.2–10 keV
4XMM J172511.3	$10.2^{+0.3}_{-0.3}$	$0.82^{+0.04}_{-0.04}$	$3.1^{+0.3}_{-0.3} \times 10^{-3}$	$3.9^{+0.6}_{-0.6} \times 10^{-5}$	70^{+6}_{-7}	$< 5 \times 10^{-6}$	< 8	$< 3 \times 10^{-6}$	< 7	2364/2299	3.56×10^{-11}
4XMM J173058.9	$1.4^{+0.6}_{-0.4}$	$0.6^{+0.3}_{-0.2}$	$5^{+3}_{-2} \times 10^{-5}$	$3^{+3}_{-2} \times 10^{-6}$	129^{+70}_{-58}	$5^{+3}_{-3} \times 10^{-6}$	236^{+105}_{-83}	$< 1 \times 10^{-6}$	< 50	69/82	1.52×10^{-12}
XMMU J173029.8	5^{+5}_{-4}	$0.0^{+0.7}_{-0.6}$	$9^{+28}_{-6} \times 10^{-6}$	$2^{+1}_{-1} \times 10^{-6}$	270^{+135}_{-135}	$< 2 \times 10^{-6}$	< 160	$2^{+3}_{-1} \times 10^{-6}$	204^{+306}_{-102}	11/17	6.70×10^{-13}
4XMM J174517.0	$2.8^{+0.3}_{-0.3}$	$1.1^{+0.1}_{-0.1}$	$9^{+2}_{-2} \times 10^{-5}$	$2.8^{+0.8}_{-0.8} \times 10^{-6}$	192^{+32}_{-31}	$1.4^{+0.8}_{-0.8} \times 10^{-6}$	78^{+34}_{-19}	$1.7^{+0.8}_{-0.8} \times 10^{-6}$	129^{+51}_{-35}	339/326	9.59×10^{-13}
4XMM J174728.9	$0.2^{+0.1}_{-0.1}$	$1.8^{+0.4}_{-0.4}$	$7^{+4}_{-2} \times 10^{-6}$	$< 4 \times 10^{-7}$	< 1500	$< 5 \times 10^{-7}$	< 2000	$< 5 \times 10^{-7}$	< 2200	16/28	4.00×10^{-14}
4XMM J173837.0	$0.9^{+0.7}_{-0.5}$	$0.8^{+0.4}_{-0.4}$	$1.1^{+1.1}_{-0.5} \times 10^{-5}$	$< 8 \times 10^{-7}$	< 351	$7^{+9}_{-7} \times 10^{-8}$	29^{+329}_{-29}	$1^{+9}_{-1} \times 10^{-7}$	59^{+320}_{-59}	23/42	2.06×10^{-13}
4XMM J174033.8	$0.9^{+0.2}_{-0.2}$	$0.5^{+0.1}_{-0.1}$	$6^{+1}_{-1} \times 10^{-5}$	$7^{+2}_{-2} \times 10^{-6}$	226^{+50}_{-46}	$4^{+2}_{-2} \times 10^{-6}$	103^{+42}_{-40}	$3^{+2}_{-2} \times 10^{-6}$	95^{+50}_{-49}	185/189	2.88×10^{-12}
4XMM J174016.0	$0.44^{+0.03}_{-0.03}$	$0.63^{+0.04}_{-0.04}$	$1.36^{+0.09}_{-0.07} \times 10^{-4}$	$9^{+2}_{-2} \times 10^{-6}$	182^{+34}_{-20}	$6^{+2}_{-2} \times 10^{-6}$	91^{+23}_{-16}	$7^{+2}_{-2} \times 10^{-6}$	135^{+27}_{-29}	736/607	5.14×10^{-12}
4XMM J174809.8	2^{+2}_{-1}	$0.3^{+0.5}_{-0.5}$	$6^{+9}_{-3} \times 10^{-6}$	$5^{+7}_{-7} \times 10^{-7}$	175^{+71}_{-71}	$< 7 \times 10^{-7}$	< 172	$3^{+14}_{-3} \times 10^{-7}$	99^{+264}_{-99}	50/48	2.96×10^{-13}
4XMM J174009.0	$0.8^{+0.3}_{-0.2}$	$0.1^{+0.1}_{-0.1}$	$6^{+2}_{-1} \times 10^{-5}$	$1.8^{+0.5}_{-0.3} \times 10^{-5}$	359^{+65}_{-120}	$1.6^{+0.6}_{-0.6} \times 10^{-5}$	265^{+78}_{-115}	$7^{+6}_{-6} \times 10^{-6}$	109^{+66}_{-56}	170/166	5.90×10^{-12}
4XMM J174954.6	$2.4^{+0.9}_{-0.7}$	$0.4^{+0.3}_{-0.3}$	$3^{+2}_{-1} \times 10^{-5}$	$2^{+1}_{-1} \times 10^{-6}$	107^{+69}_{-59}	$3^{+2}_{-2} \times 10^{-6}$	172^{+103}_{-85}	$< 3 \times 10^{-6}$	< 150	90/91	1.73×10^{-12}
4XMM J175327.8	$7^{+7}_{-5} \times 10^{-2}$	$1.3^{+0.3}_{-0.3}$	$2.8^{+0.9}_{-0.7} \times 10^{-5}$	$< 2 \times 10^{-6}$	< 774	$< 2 \times 10^{-6}$	< 660	$< 2 \times 10^{-6}$	< 751	64/41	4.29×10^{-13}
4XMM J174622.7	$4.5^{+0.9}_{-0.7}$	$0.7^{+0.2}_{-0.2}$	$2.0^{+1.0}_{-0.6} \times 10^{-5}$	$1^{+5}_{-1} \times 10^{-7}$	20^{+46}_{-20}	$1.1^{+0.6}_{-0.6} \times 10^{-7}$	207^{+76}_{-71}	$2^{+6}_{-2} \times 10^{-7}$	30^{+67}_{-30}	192/187	5.13×10^{-13}
4XMM J175452.0	2^{+3}_{-1}	$0.9^{+0.9}_{-0.7}$	$1.2^{+4.4}_{-0.9} \times 10^{-5}$	$1.4^{+0.7}_{-0.7} \times 10^{-6}$	690^{+445}_{-445}	$< 9 \times 10^{-7}$	< 206	$< 1 \times 10^{-6}$	< 529	33/41	2.68×10^{-13}
4XMM J175301.3	$0.3^{+0.5}_{-0.2}$	$0.5^{+0.3}_{-0.3}$	$5^{+3}_{-2} \times 10^{-6}$	$10^{+6}_{-6} \times 10^{-7}$	52^{+288}_{-225}	$4^{+8}_{-4} \times 10^{-7}$	105^{+189}_{-105}	$4^{+10}_{-4} \times 10^{-7}$	179^{+387}_{-179}	63/54	1.86×10^{-13}
4XMM J174917.7	$3.2^{+0.7}_{-0.6}$	$1.0^{+0.2}_{-0.2}$	$9^{+5}_{-2} \times 10^{-5}$	$2^{+1}_{-1} \times 10^{-6}$	94^{+50}_{-47}	$4^{+2}_{-2} \times 10^{-6}$	246^{+88}_{-67}	$9^{+16}_{-6} \times 10^{-7}$	52^{+112}_{-52}	107/108	1.31×10^{-12}
4XMM J175244.4	$0.1^{+0.2}_{-0.1}$	$0.7^{+0.3}_{-0.3}$	$7^{+3}_{-2} \times 10^{-6}$	$< 8 \times 10^{-7}$	< 388	$6^{+95}_{-6} \times 10^{-8}$	17^{+231}_{-17}	$1.4^{+0.9}_{-0.9} \times 10^{-6}$	796^{+443}_{-405}	29/51	2.11×10^{-13}
4XMM J174816.9	27^{+7}_{-6}	$1.3^{+0.6}_{-0.6}$	$2.0^{+4}_{-1} \times 10^{-4}$	$1.8^{+0.7}_{-0.7} \times 10^{-6}$	221^{+86}_{-86}	$1.0^{+0.7}_{-0.7} \times 10^{-6}$	109^{+76}_{-76}	$6^{+9}_{-6} \times 10^{-7}$	71^{+107}_{-71}	159/164	8.50×10^{-13}
4XMM J174445.6	$0.37^{+0.02}_{-0.02}$	$1.75^{+0.06}_{-0.06}$	$3.3^{+0.2}_{-0.2} \times 10^{-4}$	$2^{+1}_{-1} \times 10^{-6}$	80^{+39}_{-40}	$7^{+2}_{-2} \times 10^{-6}$	371^{+88}_{-76}	$2^{+1}_{-1} \times 10^{-6}$	109^{+43}_{-47}	399/412	2.03×10^{-12}
4XMM J175740.5	3^{+2}_{-1}	$0.2^{+0.4}_{-0.3}$	$1.1^{+1.1}_{-0.5} \times 10^{-5}$	$1.6^{+0.8}_{-0.8} \times 10^{-6}$	176^{+84}_{-49}	$1.3^{+0.9}_{-0.9} \times 10^{-6}$	112^{+61}_{-41}	$1.3^{+1.0}_{-1.0} \times 10^{-6}$	151^{+19}_{-64}	113/92	7.63×10^{-13}
4XMM J174906.8	21^{+1}_{-1}	$1.3^{+0.1}_{-0.1}$	$2.6^{+0.8}_{-0.6} \times 10^{-3}$	$6^{+4}_{-4} \times 10^{-6}$	40^{+15}_{-15}	$3^{+40}_{-3} \times 10^{-7}$	2^{+13}_{-2}	$3^{+44}_{-3} \times 10^{-7}$	2^{+16}_{-2}	400/442	1.12×10^{-11}
XMMU J175441.9	3^{+2}_{-1}	$0.3^{+0.4}_{-0.4}$	$1.1^{+1.3}_{-0.6} \times 10^{-5}$	$2^{+1}_{-1} \times 10^{-6}$	274^{+137}_{-137}	$3^{+14}_{-3} \times 10^{-7}$	28^{+131}_{-28}	$1^{+1}_{-1} \times 10^{-6}$	172^{+172}_{-172}	33/26	4.31×10^{-13}
4XMM J175511.6	$0.35^{+0.11}_{-0.09}$	$1.1^{+0.1}_{-0.1}$	$2.8^{+0.6}_{-0.5} \times 10^{-5}$	$1^{+6}_{-1} \times 10^{-7}$	31^{+109}_{-31}	$6^{+7}_{-6} \times 10^{-7}$	194^{+162}_{-188}	$< 1 \times 10^{-6}$	< 263	69/76	3.06×10^{-13}
4XMM J175525.0	10^{+1}_{-1}	$1.4^{+0.2}_{-0.2}$	$5^{+2}_{-2} \times 10^{-4}$	$< 1 \times 10^{-6}$	< 33	$9^{+16}_{-9} \times 10^{-7}$	34^{+36}_{-34}	$< 1 \times 10^{-6}$	< 55	171/170	1.84×10^{-12}
4XMM J175328.4	$0.43^{+0.03}_{-0.02}$	$1.40^{+0.04}_{-0.04}$	$6.3^{+0.4}_{-0.3} \times 10^{-4}$	$3^{+2}_{-2} \times 10^{-6}$	71^{+28}_{-29}	$2^{+2}_{-2} \times 10^{-6}$	28^{+26}_{-28}	$4^{+3}_{-3} \times 10^{-6}$	90^{+38}_{-36}	883/914	5.56×10^{-12}
XMMU J180140.3	3^{+2}_{-1}	$2.1^{+1.3}_{-0.9}$	$1.1^{+5.0}_{-0.8} \times 10^{-4}$	$2^{+3}_{-1} \times 10^{-6}$	670^{+1005}_{-335}	$< 4 \times 10^{-8}$	< 8	$< 6 \times 10^{-6}$	< 1500	25/27	2.31×10^{-13}

Notes. The model used for spectral fit is power-law for the continuum plus three Gaussian at 6.4, 6.7, and 6.9 keV for iron emission complex. The spectral model is convolved with a Galactic absorption component tbabs. The normalization of power-law model N_{po} is given in units of photons $\text{keV}^{-1} \text{cm}^{-2} \text{s}^{-1}$ at 1 keV and the normalization of the lines are given in units of photons $\text{cm}^{-2} \text{s}^{-1}$ in the line energy.

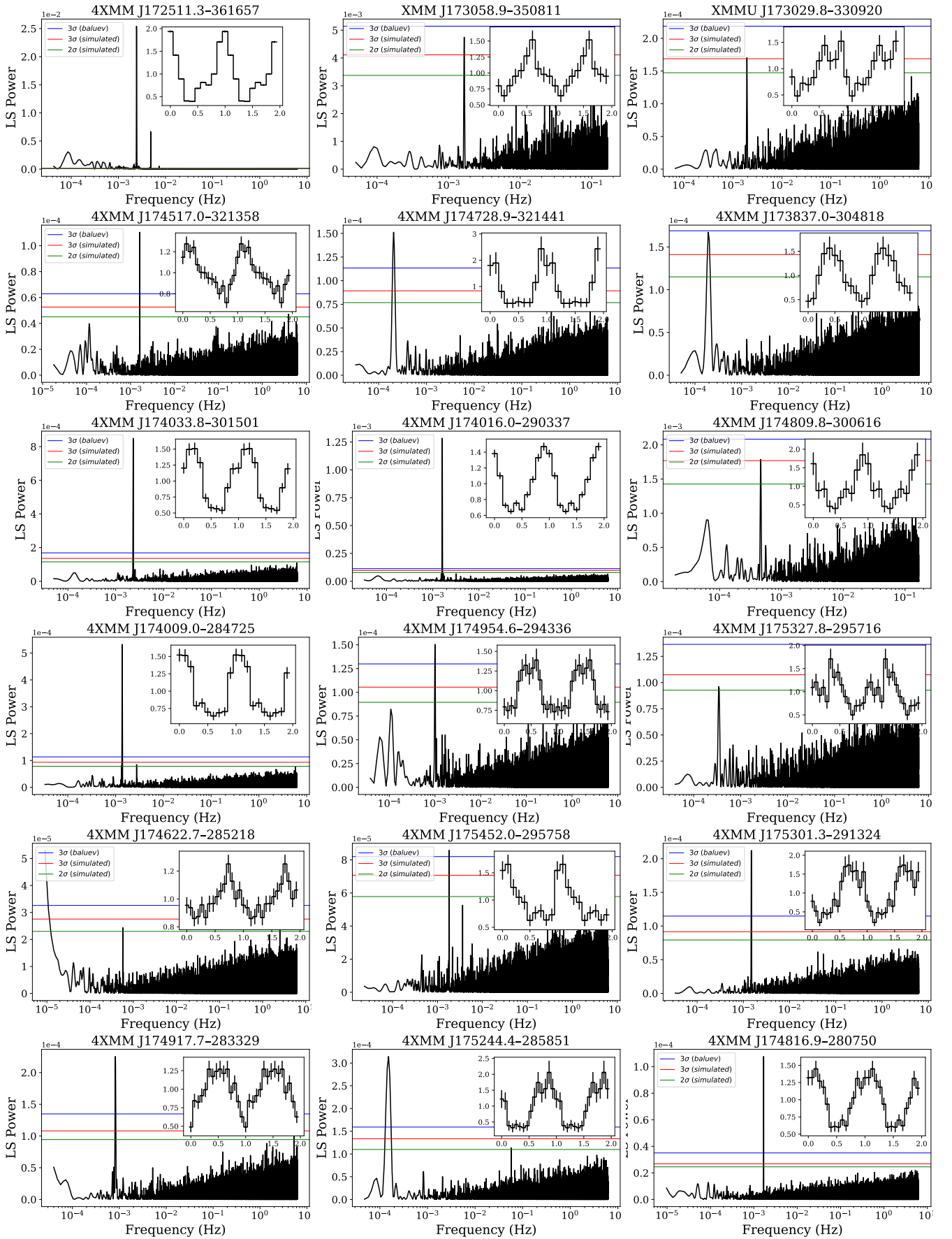


Fig. A.1: Lomb-Scargle periodogram of the sources listed in Table A.1. The periodograms are constructed using 2–10 keV EPIC-pn light curves. The horizontal green and red lines indicate the 2σ and 3σ confidence levels, respectively, computed from simulations, and the blue line indicates the false alarm probability (3σ confidence level) estimated from the analytical approximation from [Baluev \(2008\)](#). The small inset shows the folded light curve.

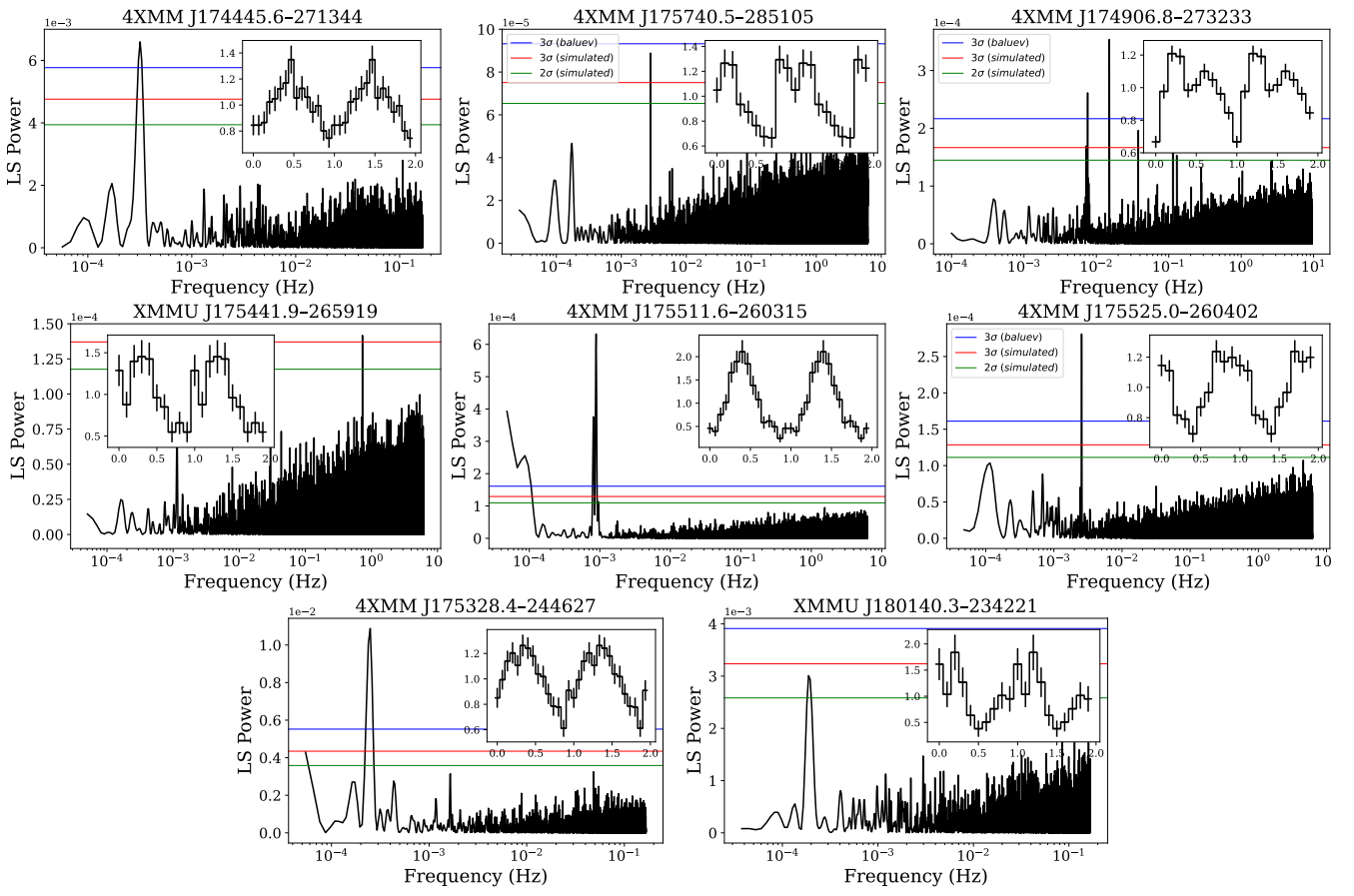


Fig. A.2: Fig. A.1 Continued.

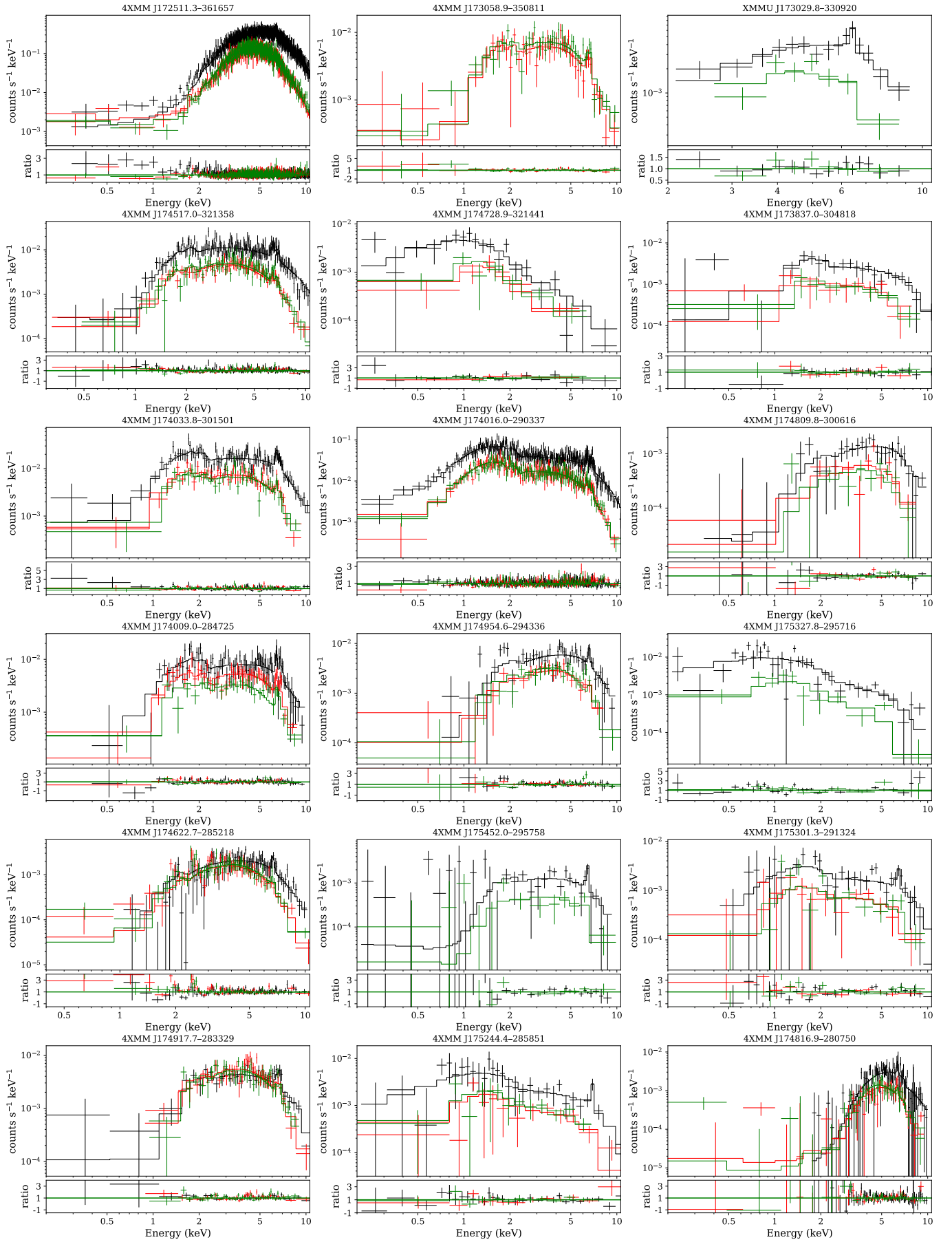


Fig. A.3: Spectral modeling of the sources in our sample using a model composed of $\text{tbabs}^*(\text{power-law}+\text{g1}+\text{g2}+\text{g3})$. The g1 , g2 , and g3 represent three Gaussian lines, at 6.4, 6.7, and 6.9 keV, respectively. The black, red, and green colors represent data from the EPIC-pn, MOS1, and MOS2 detectors, respectively.

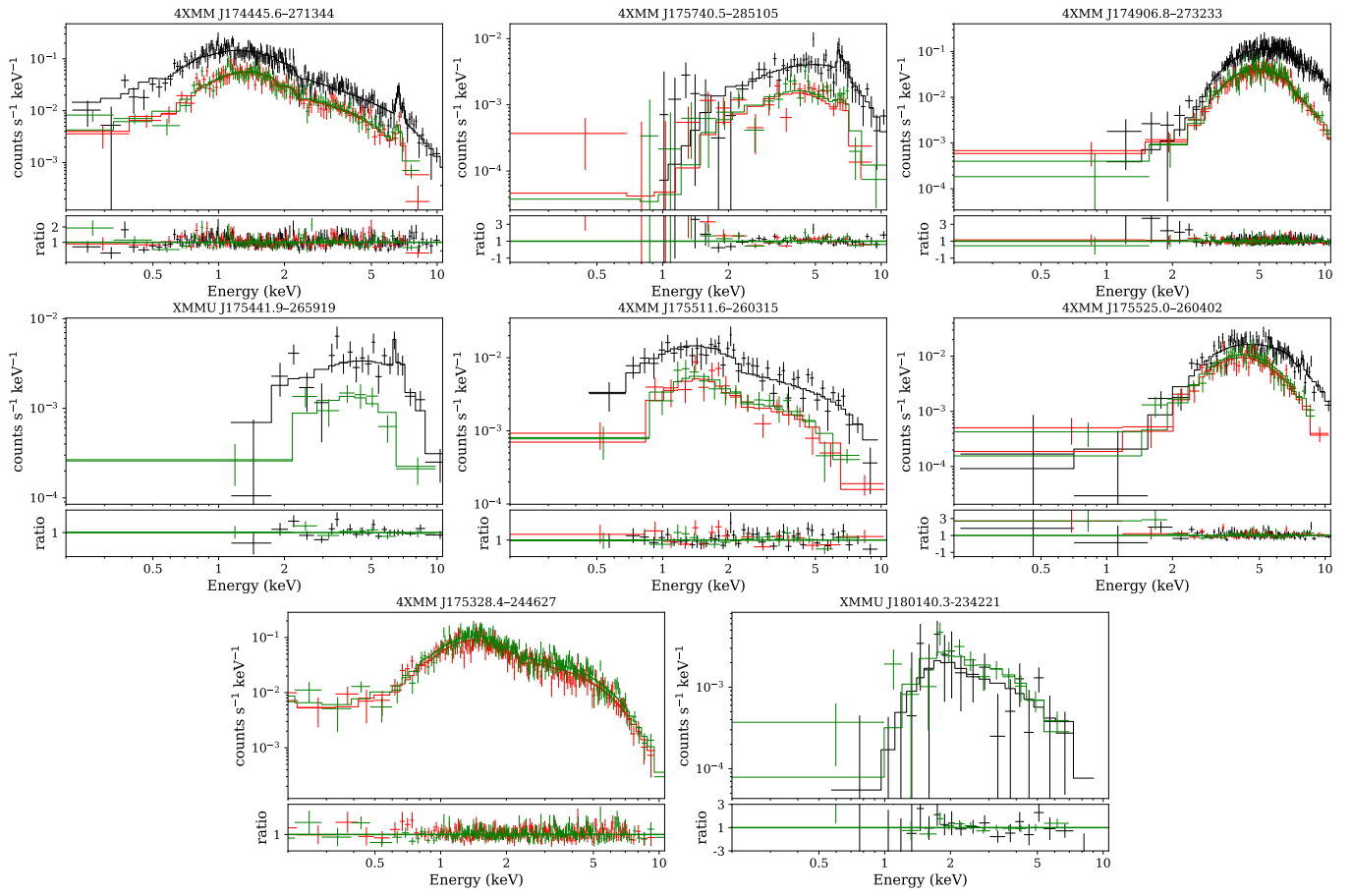


Fig. A.4: Fig. A.3 Continued.